

Linkage between Projected Precipitation and Atmospheric Thermodynamic Changes

JIAO CHEN

School of Atmospheric Sciences, Nanjing University, Nanjing, China

AIGUO DAI

Department of Atmospheric and Environmental Sciences, University at Albany, State University of New York, Albany, New York, and The National Center for Atmospheric Research, Boulder, Colorado

YAOCUN ZHANG

School of Atmospheric Sciences, Nanjing University, Nanjing, China

(Manuscript received 18 October 2019, in final form 3 June 2020)

ABSTRACT

Light–moderate precipitation is projected to decrease whereas heavy precipitation may increase under greenhouse gas (GHG)-induced global warming, while atmospheric convective available potential energy (CAPE) over most of the globe and convective inhibition (CIN) over land are projected to increase. The underlying processes for these precipitation changes are not fully understood. Here, projected precipitation changes are analyzed using 3-hourly data from simulations by a fully coupled climate model, and their link to the CAPE and CIN changes is examined. The model approximately captures the spatial patterns in the mean precipitation frequencies and the significant correlation between the precipitation frequencies or intensity and CAPE over most of the globe or CIN over tropical oceans seen in reanalysis, and it projects decreased light–moderate precipitation ($0.01 < P \leq 1 \text{ mm h}^{-1}$) but increased heavy precipitation ($P > 1 \text{ mm h}^{-1}$) in a warmer climate. Results show that most of the light–moderate precipitation events occur under low-CAPE and/or low-CIN conditions, which are projected to decrease greatly in a warmer climate as increased temperature and humidity shift many of such cases into moderate–high CAPE or CIN cases. This results in large decreases in the light–moderate precipitation events. In contrast, increases in heavy precipitation result primarily from its increased probability under given CAPE and CIN, with a secondary contribution from the CAPE/CIN frequency changes. The increased probability for heavy precipitation partly results from a shift of the precipitation histogram toward higher intensity that could result from a uniform percentage increase in precipitation intensity due to increased water vapor in a warmer climate.

1. Introduction

One of the key ingredients for precipitation formation is the cooling of an air parcel, often induced by upward motion, which in turn is determined by atmospheric buoyancy in environments without orographic or frontal lifting. To quantify atmospheric buoyancy, the convective available potential energy (CAPE) and convective inhibition (CIN) are commonly examined. CAPE and CIN represent, respectively, the positive buoyancy above and the negative buoyancy below the level of free convection (LFC) that would be experienced by a lifted parcel. CAPE is widely used to quantify atmospheric

instability, while CIN is used to measure the stability in the lower troposphere that often prevents deep moist convection from happening. Three ingredients are necessary for atmospheric moist convection to occur: moisture in the air, instability (i.e., CAPE), and lifting to overcome the stable layer (i.e., CIN) (Doswell 1987; Johns and Doswell 1992; Barkidija and Fuchs 2013; Holley et al. 2014). Therefore, atmospheric moist convection and thus convective precipitation depend on atmospheric thermodynamic conditions such as changes in CAPE and CIN, low-level humidity, and air temperature (Chen et al. 2019, 2020).

Many observational studies have revealed some relationships between precipitation rates (i.e., intensity) and CAPE or CIN on different space–time scales,

Corresponding author: Dr. Aiguo Dai, adai@albany.edu

DOI: 10.1175/JCLI-D-19-0785.1

© 2020 American Meteorological Society. For information regarding reuse of this content and general copyright information, consult the [AMS Copyright Policy](https://www.ametsoc.org/PUBSReuseLicenses) (www.ametsoc.org/PUBSReuseLicenses).

but the results are not entirely comparable. For example, [McBride and Frank \(1999\)](#) found that the diurnal rainfall is weakly but inversely correlated with CAPE at the northern end of the Gulf of Carpentaria during the monsoon season. [Adams and Souza \(2009\)](#) found a positive precipitation–CAPE correlation on the diurnal time scale over the North American monsoon region. However, [Zhang \(2002\)](#) found no apparent relationship between precipitation rates and CAPE or CIN using summertime observations from the southern Great Plains of the United States. On the daily time scale, [Monkam \(2002\)](#) found positive correlations between rainfall rates and CAPE over the Atlantic intertropical convergence zone (ITCZ) and some mountains in eastern Africa during summer of 1985, indicating a strong effect of the ITCZ and orography; whereas [Sobel et al. \(2004\)](#) found weak negative correlations between rain rates and CAPE in the western-central tropical Pacific. [Barkidija and Fuchs \(2013\)](#) also found weak correlations between daily-mean precipitation rates and CAPE over Europe using data from 20 stations during 1972–2009. On a monthly basis, [DeMott and Randall \(2004\)](#) found that precipitation anomalies had little correlation with CAPE anomalies at tropical sounding stations during 1973–99. Over the globe, [Myoung and Nielsen-Gammon \(2010a\)](#) found that the relationships between monthly precipitation and convective parameters like CAPE, CIN, and precipitable water (PW) vary with regions and seasons; they showed strong correlations between precipitation and CIN over the summer continents in the Northern Hemisphere and Australia, and between precipitation and CAPE or PW over tropical oceans. Physically, CAPE is generated by atmospheric and surface heating but is consumed during convection ([Zhang and McFarlane 1995](#)), which may or may not produce surface precipitation. While precipitation intensity during a storm may be positively correlated with the amount of CAPE available at the time of convection, when and where moist convection may occur does not entirely depend on CAPE, whose value also depends on its generation processes (i.e., atmospheric heating rates). Thus, while precipitation, especially convective precipitation, is physically related to CAPE, one should not expect a simple, one-to-one relationship between them.

The presence of CIN often complicates the relationship between precipitation intensity and CAPE, which is especially true over land where CIN is strong, as CIN can prevent convection and thus precipitation from occurring even when large CAPE exists above the LFC. Some observational and modeling studies have highlighted the importance of CIN in modulating precipitation. For

example, [Myoung and Nielsen-Gammon \(2010b\)](#) indicated that monthly precipitation was mainly modulated by CIN through the feedbacks of soil moisture in Texas summertime. [Lee and Byun \(2011\)](#) also found that daily precipitation is strongly affected by CIN rather than CAPE in South Korea using rawinsonde data from 2001 to 2008. In a modeling study, [Barthlott et al. \(2011\)](#) revealed the dependence of convective precipitation on soil moisture through CIN over complex terrain. Furthermore, [Davies \(2004\)](#) found that the frequency of tornadoes occurring with positive CAPE and strong CIN decreases with increasing CIN and height of free convection using analyzed soundings during 2001–13. However, few studies have examined the precipitation versus CAPE or precipitation versus CIN relationships in climate models.

Precipitation characteristics are expected to change under greenhouse gas (GHG)-induced global warming, with increasing intensity from more intense rainstorms but decreasing frequency due to fewer rainstorms ([Trenberth et al. 2003](#); [Sun et al. 2007](#); [Lau et al. 2013](#); [Dai et al. 2017](#)). Furthermore, the precipitation frequency decrease results from decreased light–moderate precipitation events while heavy precipitation events (including daily extremes) are projected to increase ([Sun et al. 2007](#); [Pendergrass and Hartmann 2014b](#); [Donat et al. 2016](#); [Dai et al. 2017, 2018](#)). These projected changes are qualitatively consistent with the observed decreases in light–moderate precipitation and increases in heavy precipitation ([Lau and Wu 2007](#); [Liu et al. 2009](#); [Shiu et al. 2012](#); [Ma et al. 2015, 2017](#)). Besides the above analyses of coarse-resolution data from global climate models, some recent studies also examined hourly precipitation changes from high-resolution, convection-permitting regional climate simulations. For example, using convection-permitting simulations without cumulus parameterization ([Liu et al. 2017](#)), [Prein et al. \(2017\)](#) showed large increases in very heavy precipitation during summer over most of the contiguous United States (CONUS), and [Dai et al. \(2017\)](#) found that light–moderate precipitation events would decrease while heavy precipitation events would increase over the CONUS in the future warmer climate, confirming the results from coarse-resolution global models. The same simulations were analyzed to show a decreased frequency of the weak–moderate convection and an increased frequency of the strong convection over the CONUS by [Rasmussen et al. \(2017\)](#).

The increase in heavy precipitation is expected from increased moisture convergence in future rainstorms due to increased water vapor content ([Trenberth et al. 2003](#); [Wang et al. 2016](#)), but the decreases in light–moderate precipitation and the resultant decreases in total precipitation frequency are not well explained

physically. Based on the increased dry periods between rainstorms in convection-permitting simulations of future climate, Dai et al. (2017) showed that warm-season future rainstorms would become more intense and bigger in extent and thus deplete more moisture in the atmosphere each time, while surface evaporation would increase on average at a lower rate and thus would take a slightly longer time to replenish the depleted moisture before the next rainstorm could form, leading to longer dry periods and fewer rainstorms in future warmer climates. However, how this process would preferably affect light–moderate precipitation more than heavy precipitation and thus lead to their opposite signs of change is still unclear. Pendergrass and Hartmann (2014a,b) defined two modes of change in the rain amount distribution using daily data: an increase at all rain rates (increase mode) and a shift of the distribution to higher rain rates (shift mode). Clearly, their shift mode could help explain the decreases in light–moderate precipitation, but they did not show what physical processes could cause such a shift. Thus, their results provide a statistical explanation of the model-projected precipitation changes in terms of the shift and increase modes, with limited discussions (mainly on energetic and moisture constraints) on the possible causes that might lead to such modes of change.

At the same time, climate models also project significant changes in atmospheric thermodynamic conditions, with increased CAPE over most of the globe and also stronger CIN over most land under GHG-induced global warming (Chen et al. 2020). Some studies also found increased CAPE in the future warmer climate over the United States (Diffenbaugh et al. 2013; Seeley and Romps 2015a; Rasmussen et al. 2017), eastern Australia (Allen et al. 2014), tropical areas (Seeley and Romps 2015b), and so on. Future CAPE increases primarily because of higher specific humidity, which increases latent heating above the LFC and also raises the level of neutral buoyancy, partly offset by lapse rate changes (Singh and O’Gorman 2013), whereas the CIN increase results mainly from decreased low-level relative humidity that leads to a higher lifting condensation level and a higher LFC and thus more negative buoyancy over most land (Chen et al. 2020). Given the close connection between precipitation and convection, and the similar changes with opposite signs in the weak–moderate and intense convection revealed by Rasmussen et al. (2017), we wonder whether there exists any link between the projected changes in precipitation and CAPE/CIN in global climate models, and whether the CAPE and CIN changes can help explain the decrease in light–moderate precipitation and the increase in heavy precipitation, or other processes may be needed.

In this study, we attempt to address these issues by analyzing 3-hourly precipitation data, CAPE and CIN calculated from 6-hourly output, and other fields from climate change simulations by a fully coupled model. To our knowledge, this study represents the first attempt to link the projected precipitation changes to changes in atmospheric thermodynamic conditions and try to explain the opposite changes in light–moderate and heavy precipitation using the projected CAPE and CIN changes, as well as other thermodynamic changes. The results should improve our understanding of future precipitation response to GHG forcing and how it is linked to atmospheric thermodynamic changes.

The data and analysis method are described in section 2. In section 3, we briefly evaluate the model-simulated historical precipitation frequency and analyze the projected future changes in precipitation frequency. The links between the precipitation changes and thermodynamic changes are examined in section 4. A summary and some discussion are given in section 5.

2. Data, model simulations, and methods

We used the 3-hourly precipitation data, including convective precipitation (PRC) and total precipitation P , and 6-hourly atmospheric data on 1.25° longitude \times $\sim 0.9^\circ$ latitude grids from historical and future simulations by version 4 of the Community Climate System Model (CCSM4; Gent et al. 2011), which participated in phase 5 of the Coupled Model Intercomparison Project (CMIP5; Taylor et al. 2012). The CCSM4 uses the Community Atmosphere Model version 4 (CAM4; Neale et al. 2010), which uses the cumulus scheme developed by Zhang and McFarlane (1995, hereafter ZM95) to simulate deep convection that produces most of the model’s rainfall in the tropics and a significant fraction of the total precipitation outside the low latitudes (Chen and Dai 2019). The cloud-base mass flux M_b in the ZM95 scheme is proportional to $(CAPE + CIN)$ with an adjustment time scale τ of 2 h: $M_b = (CAPE + CIN)/(\tau \times F)$, where F is the CAPE consumption rate per unit cloud-base mass flux (Neale et al. 2010). Since the mass flux M_b largely determines the moisture convergence and thus precipitation during cumulus convection, the simulated PRC is closely linked to $(CAPE + CIN)$ in CAM4, although other factors besides CAPE and CIN also affect whether PRC occurs in CAM4 at a given time and location. Clearly, this CAPE–precipitation relationship is only an approximation of that in the real world, and it may differ in ERA-Interim reanalysis and other climate models. On the other hand, the CCSM4-simulated mean CAPE and CIN show spatial and seasonal variations similar to those seen in ERA-Interim data, and its projected future

CAPE and CIN changes over the contiguous United States are comparable to those from a high-resolution model without the use of cumulus parameterization (Chen et al. 2020). Our analyses of the precipitation versus CAPE or CIN relationship below also show correlation patterns similar to those seen in ERA-Interim reanalysis data. Thus, the simple relation to CAPE and CIN used the ZM95 scheme appears to have not greatly degraded the simulation of CAPE and CIN and its relationship with precipitation in CCSM4.

We calculated the CAPE and CIN values using the 6-hourly model data for surface pressure (PS), atmospheric temperature (T), and specific humidity (q) with T and q available vertically on a hybrid sigma-pressure coordinate with a total of 26 levels. Two periods, including 1980–99 from the twentieth-century all-forcing historical simulation and 2081–2100 from the twenty-first-century simulation under the RCP8.5 high emissions scenario, were used to quantify the distributions in the historical climatology and the projected future changes under global warming. The 3-hourly near-surface specific humidity (Huss) was also analyzed in this study. Furthermore, we also used the 3-hourly precipitation data from TRMM 3B42 (derived from satellite observations; Huffman et al. 2007) averaged onto a 1.0° grid during 1998–2014 and from ERA-Interim reanalysis (Dee et al. 2011; ECMWF 2011) on a 1.0° grid during 1979–2018 to compare with the CCSM4 historical simulations. The 6-hourly ERA-Interim pressure-level data were also used to calculate CAPE and CIN during 1979–2018. In our study, we defined two categories of precipitation as light–moderate precipitation ($0.01 < P \leq 1 \text{ mm h}^{-1}$) and heavy precipitation ($P > 1 \text{ mm h}^{-1}$) and mainly focused on the frequency changes of these two kinds of precipitation. The use of the 1 mm h^{-1} threshold in this definition will become apparent when we analyze the projected changes in precipitation histograms. We show results for the annual mean and the winter and summer seasons, with an emphasis on summer. When analyzing the relationship between precipitation and CAPE or CIN, we only used half of the 3-h accumulated precipitation data that have the 6-hourly instantaneous CAPE and CIN values at the start point (for ERA-Interim) or midpoint (for CCSM4) of the selected 3-hourly precipitation periods. Tests showed that such a matching yielded the strongest correlation given the available data sampling.

Assuming an air parcel lifted from its originating level (SFC) to the LFC and then to the level of neutral buoyancy (EL), the CAPE and CIN calculations in this study use the following equations as in Chen et al. (2020):

$$\text{CAPE} = R_d \int_{p(\text{EL})}^{p(\text{LFC})} (T_{vp} - T_{ve}) d\ln(p), \quad (1)$$

$$\text{CIN} = R_d \int_{p(\text{LFC})}^{p(\text{SFC})} (T_{vp} - T_{ve}) d\ln(p). \quad (2)$$

Here R_d is the gas constant of dry air and p (hPa) is the air pressure; T_{vp} and T_{ve} (K) are the virtual temperature of the lifted parcel and the environment, respectively. The use of virtual temperature is to account for the effect of water vapor on air density (Doswell and Rasmussen 1994). Here, we only used the CAPE and CIN calculated under the reversible process with all the condensates keeping inside the parcel and with the SFC being the first model layer, and the integration stops at the pressure level of 125 hPa for ERA-Interim and the 15th model level (with a hybrid sigma value of 163.7) for CCSM4. The fixed upper bound simplifies the CAPE calculation and is high enough so that it does not affect the mean CAPE and its future CAPE change (Chen et al. 2020). The CAPE and CIN changes are similar when they are calculated using the irreversible process with all the condensates falling out of the air parcel or when using a slightly higher originating level or a different stopping level. More information about CAPE and CIN calculations (including the impact of freezing of the condensates, which is ignored here) and their changes can be found in Chen et al. (2020). For absolute stable profiles with no positive buoyancy but only negative buoyancy, which occur quite often over the mid- to high latitudes especially during the cold season (Chen et al. 2020), we set CAPE to zero and CIN to a large negative value (e.g., -4000 J kg^{-1}) since the LFC is undefined in these cases.

Three latitudinal zones including the tropics (20°S – 20°N), subtropics (20° – 40°S/N), and midlatitudes (40° – 60°S/N) over the land and ocean areas separately are used for analyzing the regional characteristics. Analytically, the regional frequency of precipitation within a specific intensity range (freq_{PR} ; % of time) as a function of both CAPE and CIN can be regarded as the product of the occurrence frequency of the events with certain CAPE and CIN ($\text{freq}_{\text{CAPE,CIN}}$; % of time) and the probability of precipitation given the occurrence frequency of the CAPE and CIN events (prob_{PR}):

$$\text{freq}_{\text{PR}} = \text{freq}_{\text{CAPE,CIN}} \text{prob}_{\text{PR}}. \quad (3)$$

We can further decompose the precipitation frequency change ($\Delta\text{freq}_{\text{PR}}$) into two terms:

$$\begin{aligned} \Delta\text{freq}_{\text{PR}} &\approx \Delta\text{freq}_{\text{CAPE,CIN}} \text{prob}_{\text{PR}_0} \\ &+ \text{freq}_{\text{CAPE,CIN}_0} \Delta\text{prob}_{\text{PR}} = \text{term1} + \text{term2}. \end{aligned} \quad (4)$$

Term1 and term2 represent the contributions from the change in the occurrence frequency of the CAPE and CIN events ($\Delta\text{freq}_{\text{CAPE,CIN}}$) and the change in the probability of precipitation under given CAPE and CIN ($\Delta\text{prob}_{\text{PR}}$), respectively. In Eq. (4), the subscript “_0” denotes the historical value. Note that the nonlinear term ($\Delta\text{freq}_{\text{CAPE,CIN}}\Delta\text{prob}_{\text{PR}}$) is neglected in Eq. (4), since it is small compared to the two linear terms as shown below. We emphasize that while term1 is explicitly related to changes in the occurrence frequency of CAPE and CIN, term2 is also likely at least partly related to thermodynamic changes, such as increased water vapor content as shown below.

3. Model projected future changes in precipitation frequency

Before analyzing the projected changes in precipitation frequency, we first briefly examine the model’s performance in simulating the mean precipitation frequency as compared to TRMM 3B42 and ERA-Interim data on comparable spatial resolution, which is critical for estimating precipitation frequency (Chen and Dai 2018). Figure 1 shows that the model captures well the annual-mean spatial variations in the occurrence frequency of both light–moderate precipitation (with maximum frequencies in the tropics and over mid- to high-latitude oceans, Figs. 1c,e) and heavy precipitation (with maxima along the tropical convergence zones and extratropical storm tracks, Figs. 1d,f) seen in ERA-Interim. However, the maximum frequencies (mainly over oceans) from TRMM satellite observations are lower for light–moderate precipitation (Fig. 1a) but larger for heavy precipitation (Fig. 1b) than both the model and ERA-Interim. This bias is mostly evident over oceans and consistent with the “drizzling” problem in many climate models (Dai 2006; Chen and Dai 2019). On the other hand, the TRMM product captures the midlatitude maximum frequency only for heavy precipitation, while it is seen for both light–moderate and heavy precipitation in the model and ERA-Interim. Surface observations (Dai 2001; Dai et al. 2007) and *CloudSat* satellite data (Ellis et al. 2009) seem to suggest that the mid- to high-latitude maximum frequency should also exist for light–moderate precipitation as well. Given the uncertainties in the TRMM data toward the midlatitudes and the consistency between the ERA-Interim and CCSM4 frequency, we conclude that the model captures the overall precipitation frequency distributions reasonably well.

Figure 2 presents the model projected changes from 1980–99 to 2081–2100 in the annual, December–February (DJF), and June–August (JJA) mean occurrence frequency of light–moderate and heavy precipitation.

Light–moderate precipitation frequency is projected to decrease over most of the globe except for the polar regions and the central equatorial Pacific (Figs. 2a,c,e). Essentially all land areas see decreased light–moderate precipitation events in JJA (Fig. 1e). The seasonal differences are most pronounced over the northern high latitudes where light–moderate precipitation increases greatly in winter but decreases in summer over the land areas (Figs. 2c,e). In contrast, the occurrence frequency of heavy precipitation increases over most of the globe except for some tropical and subtropical ocean areas and some land areas (mainly in JJA; Figs. 2b,d,f). The increase is especially large over the tropical convergence zones, the Southern Ocean, and parts of the North Pacific and North Atlantic. In general, the decreasing light–moderate precipitation frequency over most of the low- to midlatitudes and increasing heavy precipitation frequency over many parts of the globe are robust features seen in all seasons. We will mainly focus on the summertime in the following analyses.

To further analyze the precipitation frequency changes, we average and examine them over different land and ocean areas. We combine (without averaging) all the CCSM4-simulated 3-hourly precipitation data in summertime from all the grid boxes in each domain during 1980–99 or 2081–2100 to derive the histograms of precipitation (Fig. 3). As we know, the choice of the intensity bin interval affects the shape of the precipitation histogram. For example, a constant rain-rate bin interval (e.g., 1 mm h^{-1}) would yield an exponentially decreasing distribution (Dai et al. 2017), while a constant logarithmic rain-rate bin interval [e.g., $\ln(P) = 0.07$] would yield a frequency peak within the light–moderate rain rates (Pendergrass and Hartmann 2014a). Clearly, the latter captures more details for light precipitation and ensures adequate sampling of heavy precipitation. In this study, we use a constant $\log_{10}P$ bin interval in order to better describe the frequency distributions for light–moderate precipitation. Similar logarithmic rain-rate bin intervals were used in previous studies, although daily rain rates were often used (e.g., Pendergrass and Hartmann 2014a,b).

Precipitation frequency generally increases as the intensity increases from 0.01 to $\sim 0.3 \text{ mm h}^{-1}$ and then declines exponentially with intensity over the three land regions and the tropical ocean (Figs. 3a–c,e), while it decreases with intensity without any peak over the subtropical ocean and with a frequency peak around 0.02 mm h^{-1} over the midlatitude ocean (Figs. 3d,f). Frequencies for moderate–heavy precipitation are higher over the tropics than the subtropics and midlatitudes (Fig. 3). The corresponding changes in precipitation frequency from 1980–99 to 2081–2100 show large decreases for precipitation below about 1 mm h^{-1} but relatively small increases (and large

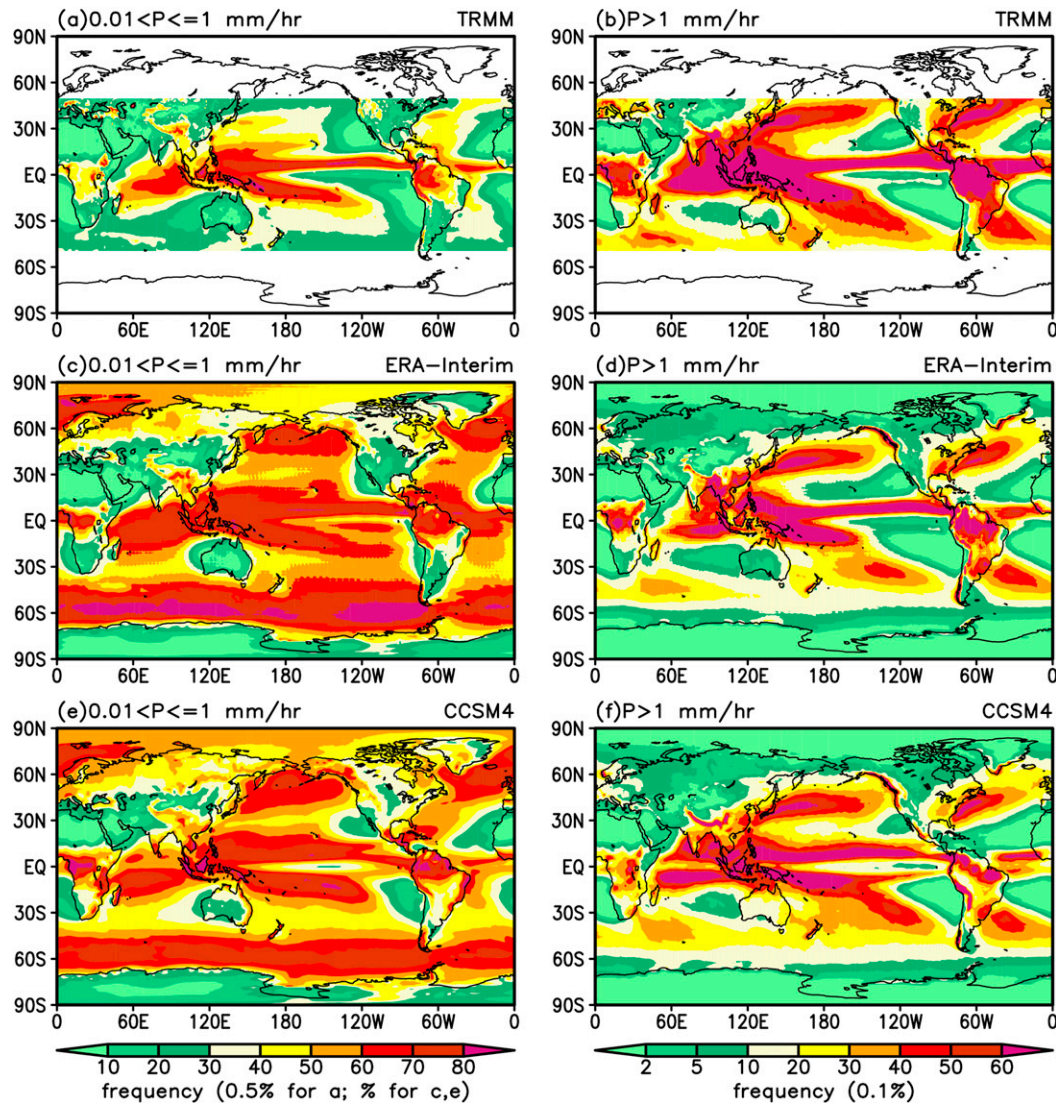


FIG. 1. Distributions of the mean occurrence frequency (% of time) of (left) light–moderate precipitation ($0.01 < P \leq 1 \text{ mm h}^{-1}$) and (right) heavy precipitation ($P > 1 \text{ mm h}^{-1}$) estimated using 3-hourly precipitation data from (a),(b) the TRMM 3B42 satellite product averaged onto a 1.0° grid during 1998–2014, (c),(d) the ERA-Interim reanalysis on a 1.0° grid during 1979–2018, and (e),(f) the CCSM4 historical simulation on a $\sim 0.9^\circ$ latitude \times 1.25° longitude grid during 1980–99.

fractional increases; not shown) for precipitation above about 1 mm h^{-1} over the land areas (Figs. 3a,c,e). These frequency changes are also true for the three ocean areas except for the very light precipitation (below $\sim 0.03 \text{ mm h}^{-1}$), which also increases (Figs. 3b,d,f).

For precipitation events lasting more than 10 h (common in the model; Chen and Dai 2019), the 1 mm h^{-1} threshold would correspond to more than 10 mm day^{-1} for daily precipitation, and this would qualify for heavy precipitation (Sun et al. 2006). Based on these considerations, we used the 1 mm h^{-1} threshold to define light–moderate ($0.01 < P \leq 1 \text{ mm h}^{-1}$) and heavy ($P > 1 \text{ mm h}^{-1}$)

precipitation. Figure 3 shows that the decreasing light–moderate precipitation frequency and increasing heavy precipitation frequency are consistent features over both land and ocean and among the different latitude zones.

4. Linkage between precipitation and thermodynamic changes

a. Relationship between precipitation and CAPE or CIN

As an example, Fig. 4a shows scatters of the selected 3-hourly convective precipitation (PRC) as a function of

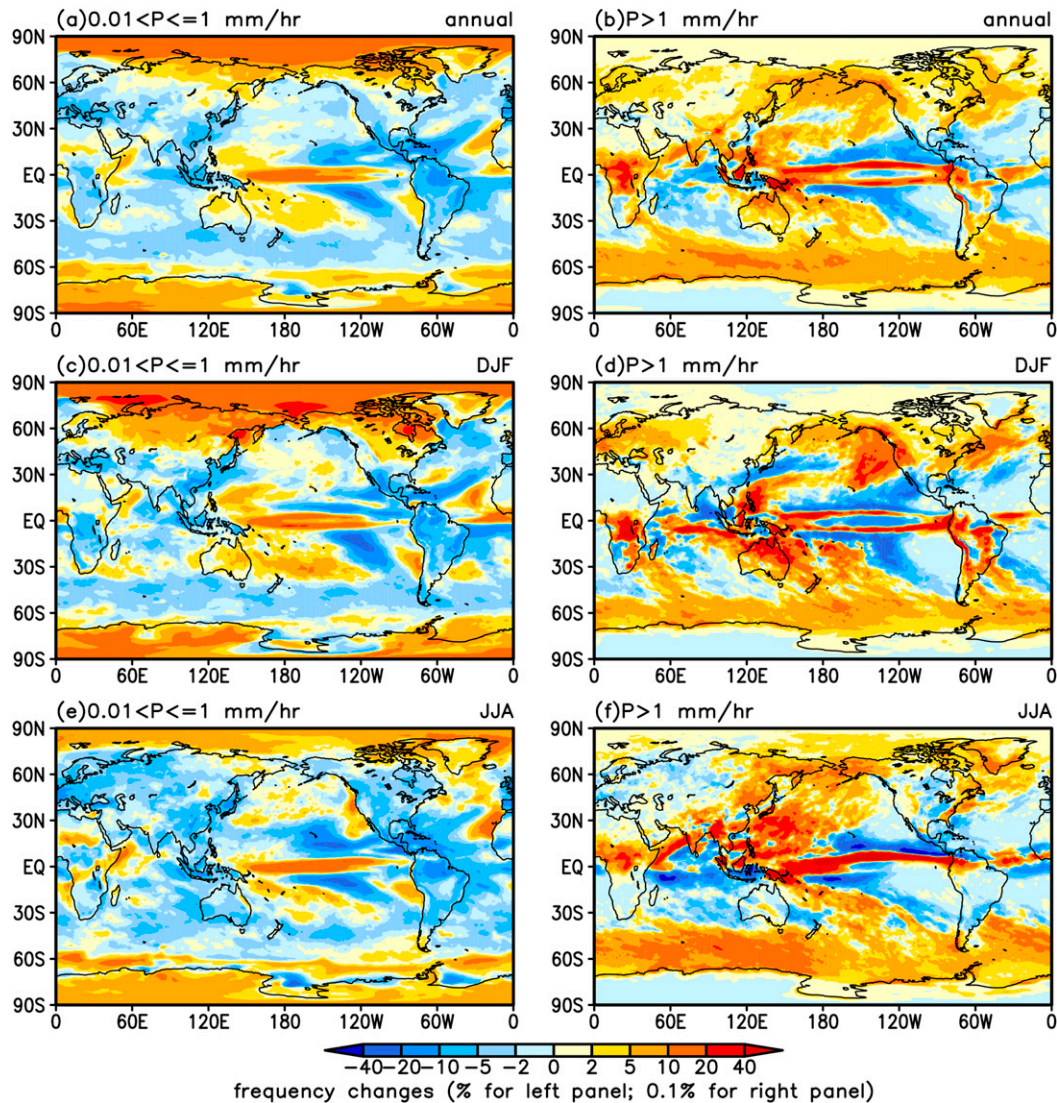


FIG. 2. Occurrence frequency changes (% of time) from 1980–99 to 2081–2100 estimated using 3-hourly precipitation data from CCSM4 historical and future simulations on a $\sim 0.9^\circ$ latitude \times 1.25° longitude grid under the RCP8.5 scenario for (left) light–moderate precipitation ($0.01 < P \leq 1 \text{ mm h}^{-1}$) and (right) heavy precipitation ($P > 1 \text{ mm h}^{-1}$) for (a),(b) the annual mean, (c),(d) DJF, and (e),(f) JJA.

the concurring CAPE and CIN over a grid box in the central United States during JJA in 1984 from ERA-Interim. Besides the absolute stable cases with CIN being set to -4000 J kg^{-1} as the LFC is unavailable in such cases (which overlap with each other in the scatterplots with same CAPE and CIN values), there are also some cases with small CAPE and zero CIN. We examined the vertical distributions of buoyancy in these cases and found that the small positive buoyancy usually occurs at the lowest levels with large negative buoyancy above. Thus, the zero CIN cannot represent the real atmospheric thermodynamic conditions in such cases. To exclude these cases in our analysis, we included

them, some of which may have medium-large CAPE, in the very strong CIN cases denoted by $\text{CIN} = -4000 \text{ J kg}^{-1}$ in Fig. 4. The correlation coefficients between PRC and CAPE or $-\text{CIN}$ (larger $-\text{CIN}$ indicates stronger CIN) or $(\text{CAPE} + \text{CIN})$ (as in the ZM95 scheme) are calculated after excluding all the $\text{CIN} = -4000$ cases. Precipitation tends to occur under weak–moderate CIN in ERA-Interim, and the correlations between PRC and CAPE or $-\text{CIN}$ are 0.66 ($p = 0.001$) or -0.30 ($p = 0.005$) (Fig. 4a).

Similar scatters from the model simulations during JJA in 1983 and 2090 are shown in Figs. 4b and 4c. For both the historical and future summers, precipitation

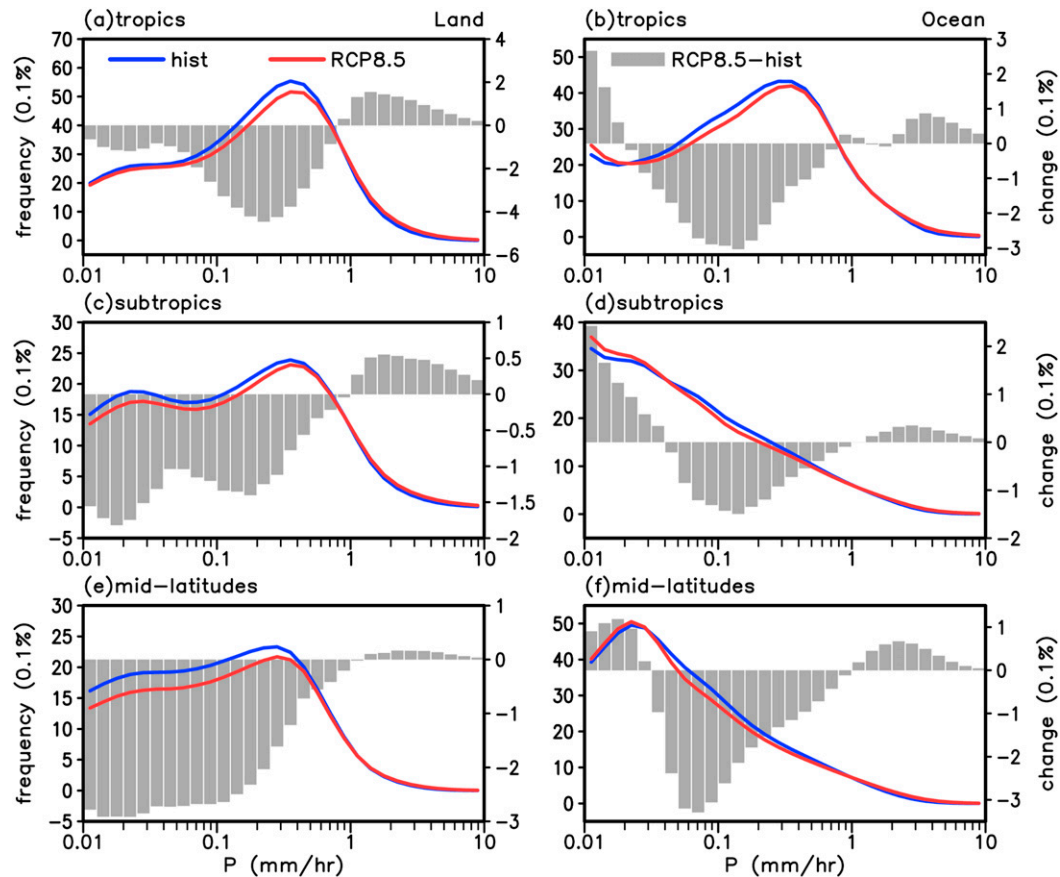


FIG. 3. Histograms (lines; left-hand y axis; 0.1% of time) of \log_{10} of CCSM4-simulated 3-hourly precipitation (for $\log_{10} P > -2 \text{ mm h}^{-1}$, with a bin size of 0.1 for $\log_{10} P$) in summer (JJA for the Northern Hemisphere and DJF for the Southern Hemisphere) during 1980–99 (black lines) and 2081–2100 (red lines) under the RCP8.5 scenario over (left) land and (right) ocean areas within three latitude zones. The histograms were derived by using all the 3-hourly precipitation data from all the grid boxes within each zone without averaging. The absolute change (0.1% of time) of the frequency from 1980–99 to 2081–2100 is shown by the gray bars on the right-hand y axis. The latitudinal zones include the (a),(b) tropics (20°S–20°N), (c),(d) subtropics (20°–40°S/N), and (e),(f) midlatitudes (40°–60°S/N).

tends to occur under strong CAPE and weak–moderate CIN conditions, while time periods with large CIN usually have little precipitation (Figs. 4b,c), which is also true in ERA-Interim (Fig. 4a). There are also fewer precipitation events in the future summer associated with the stronger CIN despite the increased CAPE (Fig. 4c). The correlation coefficients between PRC and CAPE are 0.40 ($p = 0.001$) and 0.44 ($p = 0.001$) for the historical and future summer, respectively, indicating a significant positive relationship between them. The correlation coefficient between PRC and $-CIN$ is significant for the future summer with a value of -0.42 ($p = 0.001$). These significant correlations indicate that strong CIN would inhibit convection and thus reduce PRC, especially for the future period.

The time series of the sum of CAPE and CIN (not shown) also revealed a positive relationship with PRC in both ERA-Interim and model simulations (their

correlation coefficients are shown in Fig. 4 as $r3$). Since CIN is a factor of 2–5 smaller than CAPE in Fig. 4 excluding $CIN = -4000$ cases, the variations in (CAPE + CIN) largely follow those of CAPE alone, leading to similar correlations with PRC for CAPE and (CAPE + CIN). We also examined the total precipitation and found similar relationships with CAPE and CIN, because PRC dominates the total precipitation over this location, especially in summertime (not shown). Chen and Dai (2019) also revealed that PRC accounts for most of the total precipitation in low latitudes in CAM4. In the following, we will mainly focus on the total precipitation (or simply precipitation).

To examine the relationship over other locations, Fig. 5 shows the global distributions of the correlation coefficients between annual precipitation frequency or mean intensity and the concurring CAPE or CIN for precipitation larger than 0.01 mm h^{-1} in ERA-Interim.

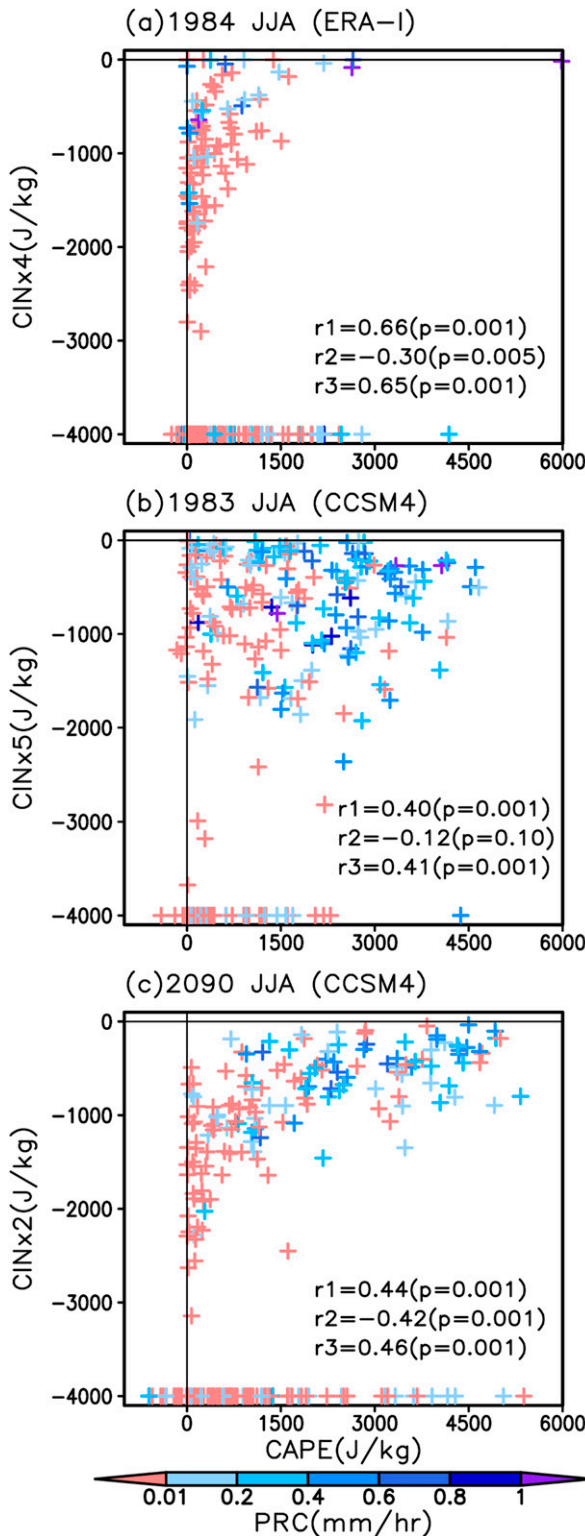


FIG. 4. Scatterplots for the 3-hourly convective precipitation (PRC; colored pluses; the colors denote PRC intensity ranges in mm h^{-1}) with 6-hourly CAPE and CIN values at the (a) start point or (b),(c) midpoint of the selected 3-hourly precipitation periods during JJA in 1984 from ERA-Interim reanalysis (a) and in 1983 in

Both precipitation frequency and mean intensity are positively correlated with the corresponding mean CAPE values over most of the globe (Figs. 5a,c). On the other hand, more than half of the areas show (mostly weak) negative correlations between precipitation frequency and $-CIN$ (Fig. 5b), while most areas show positive correlations between precipitation intensity and $-CIN$ (Fig. 5d), indicating that stronger CIN often leads to heavier precipitation but fewer precipitation events.

The model captures the broad correlation patterns seen in ERA-Interim, with stronger positive correlations with CAPE over the Pacific and other tropical oceans (Figs. 6a,c), which may be related to the specific closure assumption in the ZM95 scheme used in CCSM4. The precipitation frequency is insignificantly correlated with $-CIN$ over most areas except the equatorial central and western Pacific with positive correlations and a few other regions (Fig. 6b). The mean precipitation intensity is also positively correlated with the mean $-CIN$ over the tropical oceans (Fig. 6d), suggesting that heavier precipitation tends to occur under stronger CIN. Physically, this seems to suggest that strong CIN would suppress convection and allow CAPE above the LFC to accumulate, leading to intense convection when an air parcel does get to the LFC. Thus, a strong precipitation (including frequency and intensity) versus CAPE relationship on the inter-annual time scale exists over most of the globe for both ERA-Interim and CCSM4, and CIN mainly modulates precipitation intensity especially over low- to midlatitude oceans. These analyses suggest that there may exist some linkage between model projected changes in precipitation and thermodynamic conditions such as CAPE and CIN.

b. Regional precipitation changes explained by thermodynamic changes

We first present the historical frequency distributions and the future percentage changes of CAPE and CIN over different domains in Fig. 7 to compare with the precipitation histograms and changes shown in Fig. 3. The exponentially decreasing frequency with increasing

←

(b) and 2090 in (c) from CCSM4 simulations under the historical and RCP8.5 scenario for a grid box centered at 40°N , 100°W over the United States. The CIN values (excluding the $CIN = -4000$ cases; see text for details) were multiplied by a factor of 4 in (a), 5 in (b), and 2 in (c) in order to use the same y-axis scale. The correlation coefficients between PRC and CAPE (r_1) or $-CIN$ (r_2) or $CAPE + CIN$ (r_3) (excluding the $CIN = -4000$ cases) are shown in each panel with the attained significance level in the parentheses.

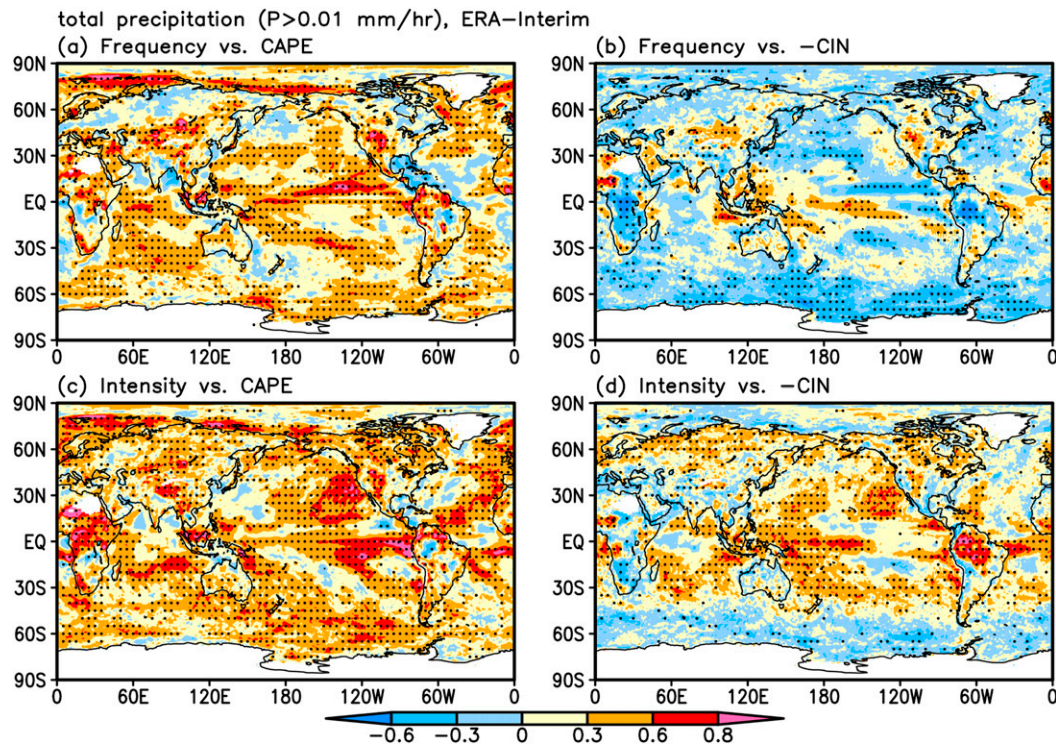


FIG. 5. Distributions of the correlation coefficients between annual precipitation (top) frequency or (bottom) mean intensity and the concurring (a),(c) CAPE or (b),(d) -CIN averaged over the time periods with precipitation larger than 0.01 mm h^{-1} during 1979–2018 from ERA-Interim reanalysis. Dots indicate statistically significant correlations at the 95% confidence level based on a Student's t test.

values for both CAPE and CIN is seen over most of the domains (Fig. 7). One exception is that CAPE over the tropical ocean (Fig. 7c) and, to a lesser degree, tropical land (Fig. 7a), has a relatively large frequency around 1500 J kg^{-1} (Fig. 7c). The frequency of CAPE or CIN is projected to decrease for small CAPE or CIN events but increase for large CAPE or CIN events in the future over most of the domains (Fig. 7), except for CAPE over the midlatitude oceans, which show increased frequencies for weak CAPE events (Fig. 7c). These similar changes in the frequency between precipitation and CAPE or CIN suggest a possible role of the CAPE and CIN changes in the precipitation frequency changes. The frequency distributions and projected future changes of CAPE and CIN over different land and ocean areas have already been examined by Chen et al. (2020) using 2D histograms as a function of both CAPE and CIN; they found that cases with weak CAPE and/or CIN would decrease greatly while cases with moderate–strong CAPE and CIN would increase, as increased T , q , and RH changes would shift many of the weak-CAPE and weak-CIN cases into moderate–strong CAPE/CIN cases. We will also examine the precipitation frequency changes over different areas

as a function of both concurring CAPE and CIN in the following analyses.

Precipitation frequencies as a function of both CAPE and CIN over summer land areas during 1980–99 and its projected changes from 1980–99 to 2081–2100 are presented in Figs. 8 and 9 (as color shading) for light–moderate and heavy precipitation, respectively, together with the associated mean precipitation intensity for historical climate (as contours). Over tropical land areas, light–moderate precipitation occurs most frequently when CIN is small (greater than about -30 J kg^{-1} , and CAPE can be as large as 2000 J kg^{-1}), or when both CIN and CAPE (less than about 200 J kg^{-1}) are small (Fig. 8a). Light–moderate precipitation frequencies over the subtropical and midlatitude land areas show similar dependence on CAPE and CIN, but are concentrated at lower CIN values for the subtropics (Fig. 8c) and over cases with both low CIN and low CAPE for the midlatitudes (Fig. 8e). For all the regions, light–moderate precipitation events decrease greatly under conditions with low CIN and/or low CAPE, but increase slightly under conditions with moderate–strong CAPE and/or moderate–strong CIN, although the increased frequency in the subtropics and midlatitudes occurs further toward large CAPE values

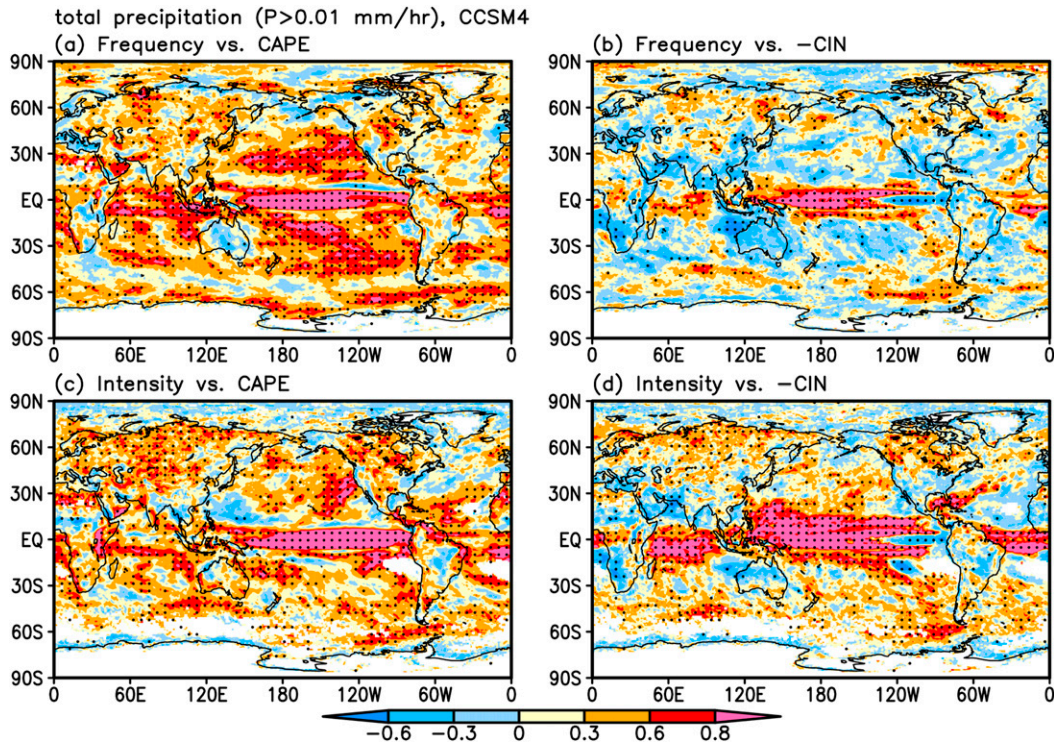


FIG. 6. As in Fig. 5, but using CCSM4 historical simulations during 1980–99.

compared with the tropical case (Figs. 8b,d,f). Moreover, the historical mean intensity distributions indicate that relatively large rain rates occur under conditions with stronger CAPE and weaker CIN, where the frequency tends to increase. These distribution patterns of the light–moderate precipitation frequency and their changes are similar to those of the CAPE and CIN shown in Chen et al. (2020), presumably because light–moderate precipitation events account for a large fraction of time (e.g., 54.4% over tropical land, 21.7% over subtropical land, and 16.8% over midlatitude land). When integrated over all the CAPE and CIN bins, the total frequency changes are all negative in Fig. 8 because the decreases under small CAPE and CIN dominate over the increases under moderate–strong CAPE and CIN. The decreases of the light–moderate precipitation frequency are consistent with the frequency changes shown in Fig. 3.

For heavy precipitation, the mean frequency distribution is similar to that for light–moderate precipitation but with much lower frequencies (left panels in Fig. 9). However, the projected changes differ from those for light–moderate precipitation, as the increased frequency under moderate–strong CAPE and/or CIN overwhelms the decreased frequency under small CAPE and CIN over the tropical and subtropical land areas, resulting in positive frequency changes when integrated over all cases (Figs. 9b,d). We also examined the frequency

changes of heavy precipitation defined with a larger threshold (i.e., $P > 2$ or 3 mm h^{-1}) and found increased frequency under all CAPE and CIN values (not shown). The frequency changes for heavy precipitation over midlatitude land (Fig. 9f) is relatively small, and the omitted (mostly) increased frequency outside the plotted CAPE and CIN ranges (i.e., the frequency change is 0.15% for $CAPE > 3000$ $J kg^{-1}$ and/or $CIN < -150$ $J kg^{-1}$) may be responsible for the negative integrated frequency change shown on Fig. 9f.

We then examine the precipitation probability (%) and its change given the occurrence frequency of CAPE and CIN for light–moderate (Fig. 10) and heavy (Fig. 11) precipitation, respectively. Light–moderate precipitation has the highest probability to occur under strong CAPE and weak CIN conditions and is least likely to happen under weak CAPE and strong CIN condition for all the three land regions (Figs. 10a,c,e). The probability of light–moderate precipitation is projected to decrease under most of the CAPE and CIN conditions, especially for the low CAPE conditions over the tropical land (Figs. 10b,d,f). For tropical and subtropical land, heavy precipitation has relatively high probability to occur around CAPE of 600 $J kg^{-1}$ and CIN of -90 $J kg^{-1}$ besides the high values with small CIN (Figs. 11a,c), while the probability over the midlatitudinal land shows relatively high values under strong CAPE (around 2400 $J kg^{-1}$) and

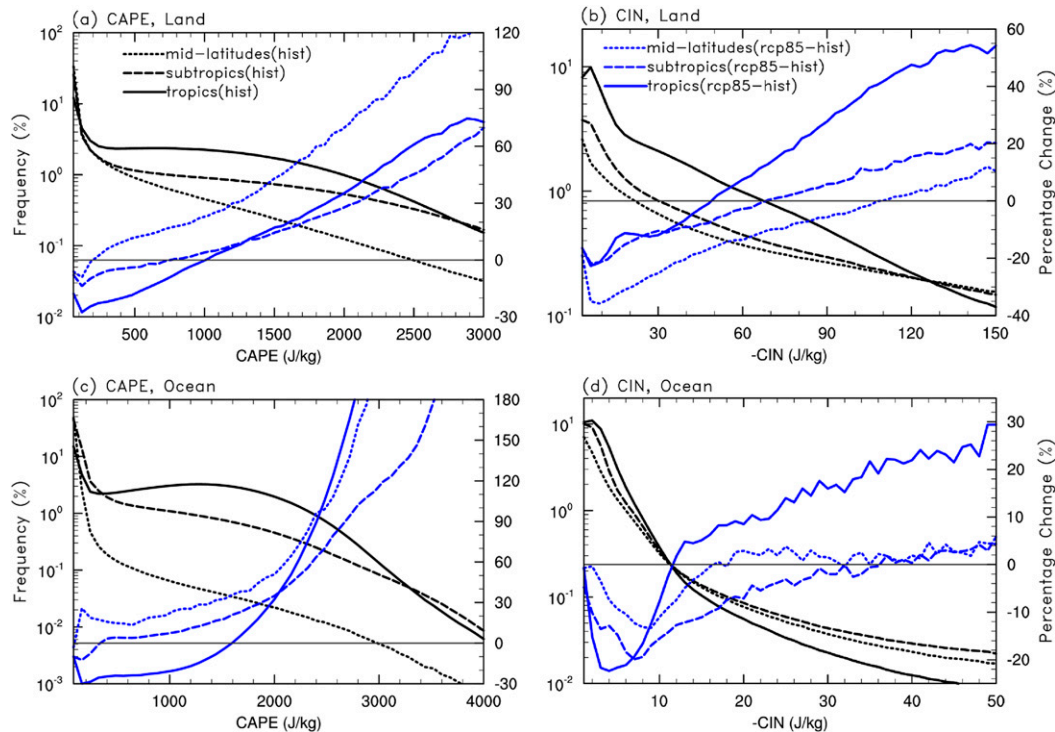


FIG. 7. Histograms (black lines; left-hand y axis; % of time) of CCSM4-simulated 6-hourly (left) CAPE and (right) $-CIN$ in summer (JJA for the Northern Hemisphere and DJF for the Southern Hemisphere) during 1980–99 over (a),(b) land and (c),(d) ocean areas within three latitude zones. The histograms were derived by using all the 6-hourly CAPE/CIN from all the grid boxes within each zone without averaging. The percentage change of the frequency from 1980–99 to 2081–2100 under the RCP8.5 scenario is shown by the blue lines on the right-hand y axis. The latitudinal zones include the tropics ($20^{\circ}S$ – $20^{\circ}N$; solid lines), subtropics (20° – $40^{\circ}S/N$; long-dashed lines), and midlatitudes (40° – $60^{\circ}S/N$; short-dashed lines). The horizontal thin line indicates the zero change. A fixed bin number of 50 was used for all the panels, with the bin interval being 60, 3, 80, and 1 $J\ kg^{-1}$ in (a)–(d), respectively.

low CIN (around $-20\ J\ kg^{-1}$) conditions (Fig. 11e). In contrast to the decreasing probability for light–moderate precipitation, the probability of heavy precipitation increases under most CAPE and CIN conditions, especially for the tropics and subtropics (Figs. 11b,d,f).

Figure 12 shows the contributions by the two decomposed terms [Eq. (4)] to the precipitation frequency change over tropical land areas for the light–moderate and heavy precipitation. Their sum (Figs. 12e,f) shows changes similar to the model-projected changes in precipitation frequency (Figs. 8b and 9b). This suggests that the decomposition method [Eq. (4)] works well and the nonlinear term is small. As term1 represents the precipitation frequency change due to changes in the occurrence frequency of CAPE and CIN and term2 represents the change due to changes in precipitation probability under given CAPE and CIN , Fig. 12 shows that for light–moderate precipitation, both the decreased frequency under weak CAPE and CIN conditions and increased frequency under strong CAPE and CIN (Fig. 12e) result mainly from the occurrence frequency change of CAPE

and CIN (Fig. 12a), which decrease greatly for weak CAPE and CIN cases but increase for moderate–strong CAPE and CIN cases (Chen et al. 2020). In contrast, for heavy precipitation, both terms contribute significantly to the projected frequency changes (Figs. 12b,d,f). The frequency decrease under weak CAPE and CIN (due to decreased occurrence frequency of weak CAPE and CIN) is largely offset by the increase caused by the increased precipitation probability under given CAPE and CIN . The net result is a small decrease in heavy precipitation frequency under weak CAPE and CIN but large increases under moderate–strong CAPE and CIN (Fig. 12f). The decomposition results for the subtropical and midlatitudinal land areas (not shown) are qualitatively similar to those for the tropical land areas.

We also examined the precipitation frequency and probability and their projected changes as a function of both CAPE and CIN for the ocean areas within the three domains (not shown), and the decomposition

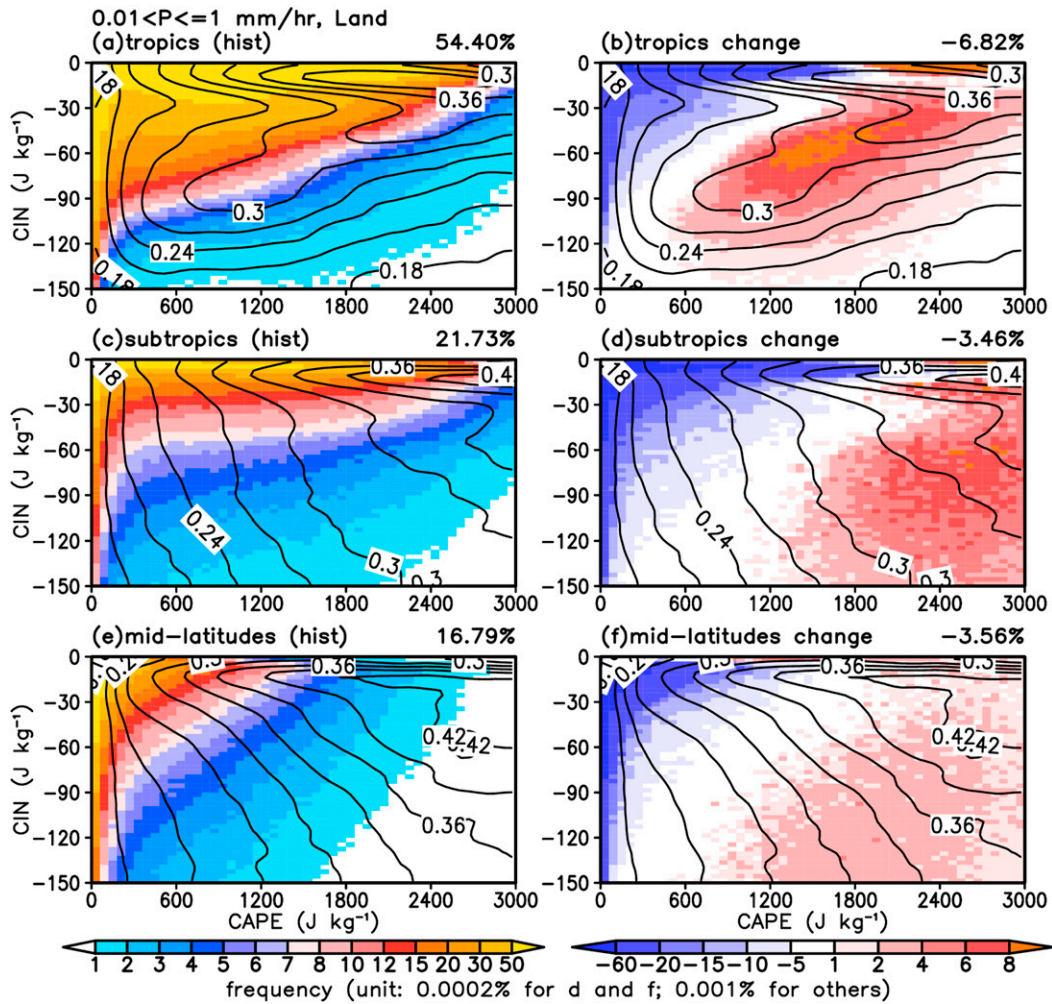


FIG. 8. (left) Light–moderate precipitation ($0.01 < P \leq 1 \text{ mm h}^{-1}$) frequency (color shading; % of time) and the 1980–99 mean intensity (contours; mm h^{-1}) as a function of both CAPE and CIN over land in summer (JJA for the Northern Hemisphere and DJF for the Southern Hemisphere) during 1980–99 in three different latitudinal zones, and (right) the corresponding changes from 1980–99 to 2081–2100 using selected 3-hourly precipitation data (which have the 6-hourly CAPE and CIN values at the midpoint of the selected 3-hourly precipitation periods) from the CCSM4 simulations under the historical and RCP8.5 scenario. The regions include the (a),(b) tropics (20°S – 20°N), (c),(d) subtropics (20° – 40°S/N), and (e),(f) midlatitudes (40° – 60°S/N). A fixed bin number of 50 was used for both CAPE and CIN. The total frequency or its change averaged over all bins is shown on the top-right corner of each panel.

results for tropical oceans are shown in Fig. 13. The frequency and its future changes of light–moderate precipitation over ocean are also similar to those of the CAPE and CIN occurrence frequency (cf. Fig. 6 in Chen et al. 2020), which differ slightly from those over land partly due to different CAPE and CIN values. One difference from land is that CIN is weak (often $> -50 \text{ J kg}^{-1}$) over ocean while oceanic CAPE is stronger. The large decreased frequency under weak CAPE overwhelms the increased frequency under strong CAPE and results in an overall decrease in light–moderate precipitation over ocean. For heavy precipitation, the increased frequency

under strong CAPE dominates over the decreased frequency under small CAPE and results in an overall increase. Light–moderate precipitation is most likely to occur under large CAPE and small CIN conditions over all the ocean areas and this probability is projected to decrease over tropical oceans. The probability of heavy precipitation has a maximum centered around CAPE of 800 J kg^{-1} and CIN of -15 J kg^{-1} for the tropical and subtropical oceans and this probability would increase in the future. The decomposition results over the tropical oceans also show opposite contributions from the precipitation probability change to the precipitation frequency

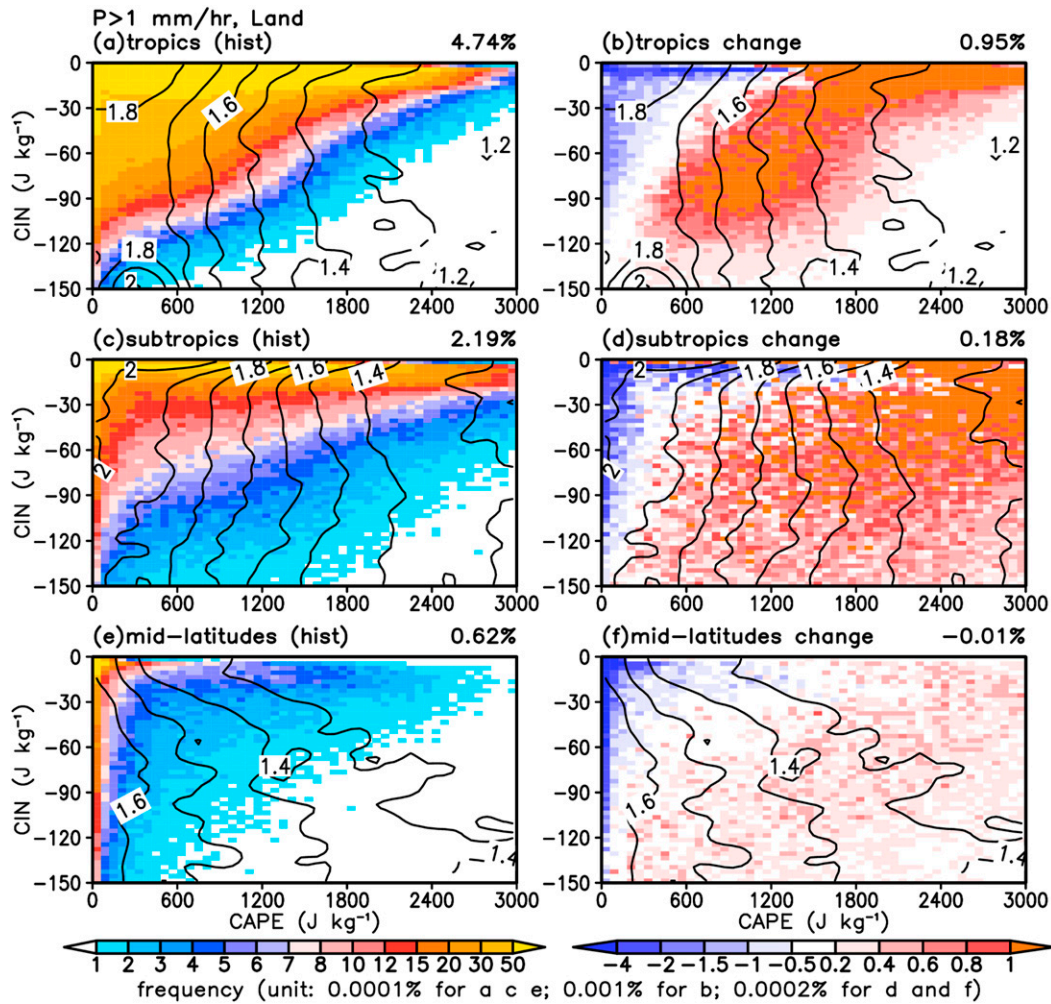


FIG. 9. As in Fig. 8, but for heavy precipitation larger than $1\ mm\ h^{-1}$.

change between light–moderate and heavy precipitation (Fig. 13). The decreased light–moderate precipitation frequency under low-moderate CAPE (Fig. 13e) results from both the decreased events with low-moderate CAPE (Fig. 13a) and the decreased precipitation probability under such CAPE values (Fig. 13c), whereas the increases caused by the increased heavy precipitation probability (Fig. 13d) offset most of the decreases caused by decreased cases with low–moderate CAPE (Fig. 13b) and enhance the frequency increases under high CAPE and moderate CIN (Figs. 13d,f). The decomposition results for other ocean areas (not shown) are also qualitatively similar.

c. Impact of water vapor increases on precipitation distribution and probability

The above analyses suggest that the increased probability for heavy precipitation under given CAPE and CIN is important to the projected increase in heavy

precipitation frequency, and this increased probability of heavy precipitation does not depend on the CAPE or CIN values (Figs. 11b,d,f). This means that heavy precipitation is more likely to occur in the future than today regardless of the CAPE and CIN conditions. A positive feedback between tropical convection and water vapor was revealed by Tompkins (2001), who indicated a critical role of lower-atmospheric moisture in controlling tropical convection through a modeling study. Trenberth et al. (2003) argued that precipitation intensity should depend on the low-level moisture convergence, which is proportional to water vapor content. Dai et al. (2017) also showed that increased water vapor would lead to increased heavy precipitation. In observational analyses, Huang et al. (2019) found that the increase in precipitation extremes occurs along with large atmospheric moisture. These studies seem to suggest that the increased heavy precipitation and its probability under given CAPE and

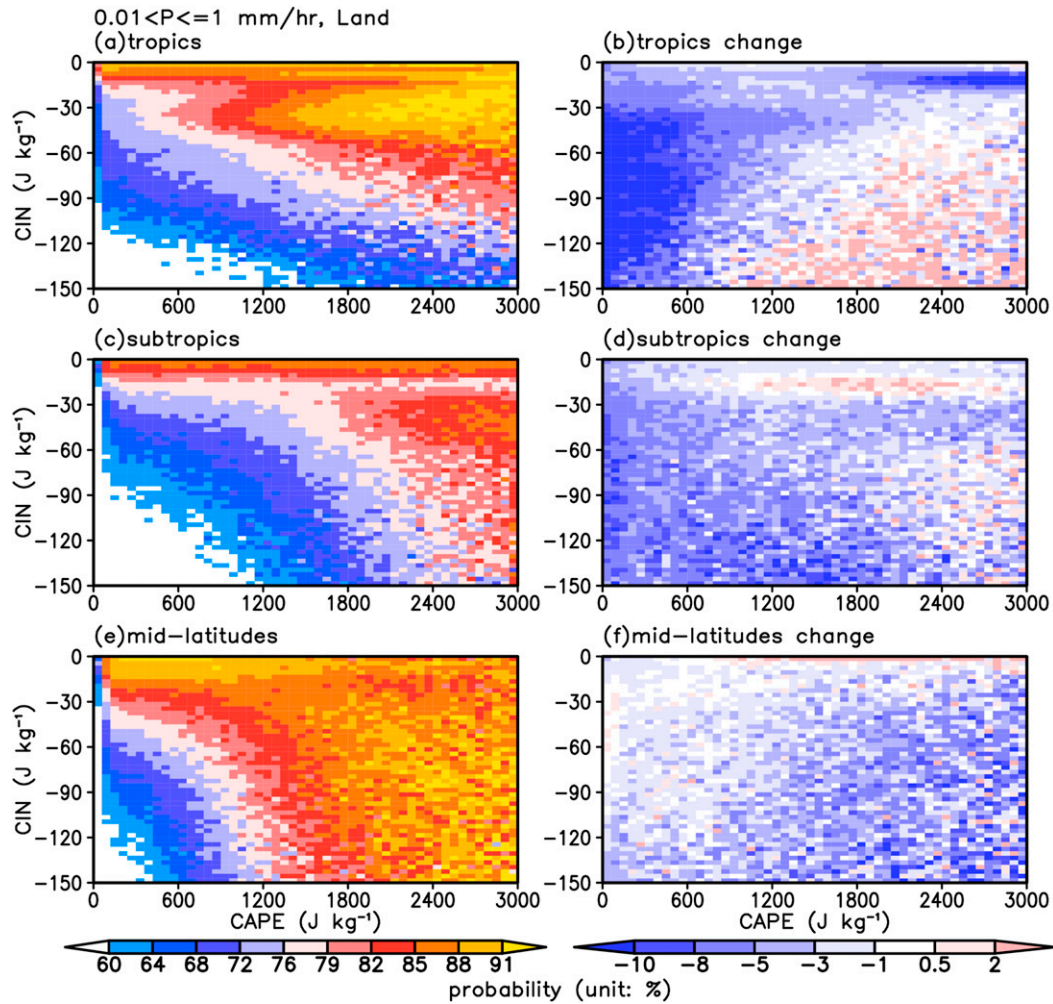


FIG. 10. (left) The probability (% chance) of light-moderate precipitation, defined as $0.01 < P \leq 1 \text{ mm h}^{-1}$, given the occurrence of the CAPE and CIN values over land in summer (JJA for the Northern Hemisphere and DJF for the Southern Hemisphere) during 1980–99 in different domains, and (right) the corresponding changes in this probability from 1980–99 to 2081–2100 from the CCSM4 simulations under the historical and RCP8.5 scenario. The regions include the (a),(b) tropics (20°S – 20°N), (c),(d) subtropics (20° – 40°S/N), and (e),(f) midlatitudes (40° – 60°S/N). A fixed bin number of 50 was used for both CAPE and CIN.

CIN conditions in the future might be related to atmospheric moisture changes.

Figure 14 shows the historical and future mean probability (contours) and their difference (color shading) of the near-surface specific humidity (Huss) as a function of CAPE and Huss values. As expected, large CAPE tends to occur with high Huss. This is consistent with the notion that CAPE would increase with increased specific humidity of the lifting level (Chen et al. 2020). Furthermore, cases with higher Huss are more likely to happen in the future than today for any given CAPE (Fig. 14). Therefore, Huss would increase in the future even under a fixed CAPE value, and this increased Huss would lead to increased precipitation intensity through increased moisture convergence (Trenberth et al. 2003). In other words,

under a given CAPE, the increased Huss would increase precipitation intensity and thus the probability of heavy precipitation, as some of today's moderate precipitation events may become strong enough to join the heavy precipitation category in the future climate.

To quantify the direct impact of increased water vapor on precipitation intensity while ignoring its impact through other processes such as changes in the occurrence frequency of CAPE and CIN, following Dai et al. (2017) we assume that the same precipitation events of the current climate would occur in the future climate but at an intensity increased by 7% per 1 K warming for all the events as a result of increased moisture convergence due to increased water vapor. For example, over a period of 100 days with certain CAPE and CIN values at a given

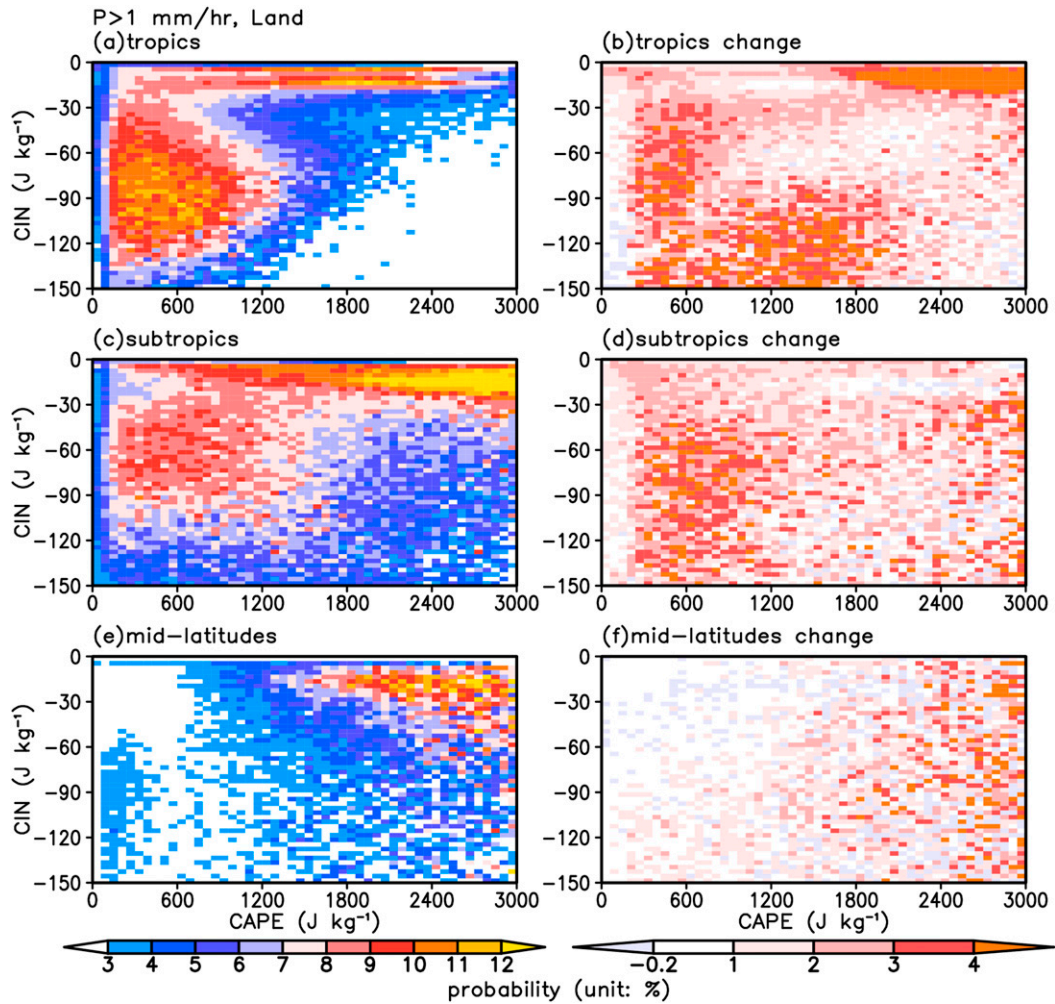


FIG. 11. As in Fig. 10, but for precipitation larger than 1 mm h⁻¹.

location, there may be 20 rainy days, thus freq_{PR} , $\text{freq}_{\text{CAPE,CIN}}$, and prob_{PR} in Eq. (3) would be 20, 100, and 20/100, respectively, for both the historical and future climates. Thus, this only represents the impact from a redistribution of the precipitation histogram due to the uniform percentage increase in the intensity of all the historical precipitation events under constant occurrence frequency of CAPE and CIN, with little change in the total number of precipitation events. The frequency shift between the light-moderate and heavy precipitation may help explain the different probability changes shown in Figs. 10 and 11, as it represents their probability changes under constant occurrence frequency of CAPE and CIN. Note that the water vapor increase may change the CAPE and CIN values but their occurrence frequency would still remain the same (e.g., at 100 days in our example). Due to the fact that some of the very light drizzling events (i.e., $P \leq 0.01 \text{ mm h}^{-1}$) can become strong enough to enter the lightest precipitation

bins after the universal percentage intensity increase, the total number of precipitation events may increase even though we assumed that the same precipitation events occur in this calculation.

The result is shown in Fig. 15, which shows that the water vapor-based scaling leads to a shift of the histograms toward the right-hand side (i.e., larger intensity) over the different land and ocean regions. A frequency peak around the precipitation intensity of 0.3 mm h^{-1} is seen over the three land regions (Figs. 15a,c,e) and the tropical ocean (Fig. 15b) in current climate, and this peak shifts toward higher intensity with little change in the shape after the scaling, resulting in generally decreased frequency on the left side (i.e., for light-moderate precipitation) of the peak and increased frequency on the right side (i.e., for moderate-heavy precipitation) of the peak. Dai et al. (2017) did a similar analysis but found increased frequency for all types of precipitation because they used a constant rain-rate (instead of $\log_{10}P$) bin

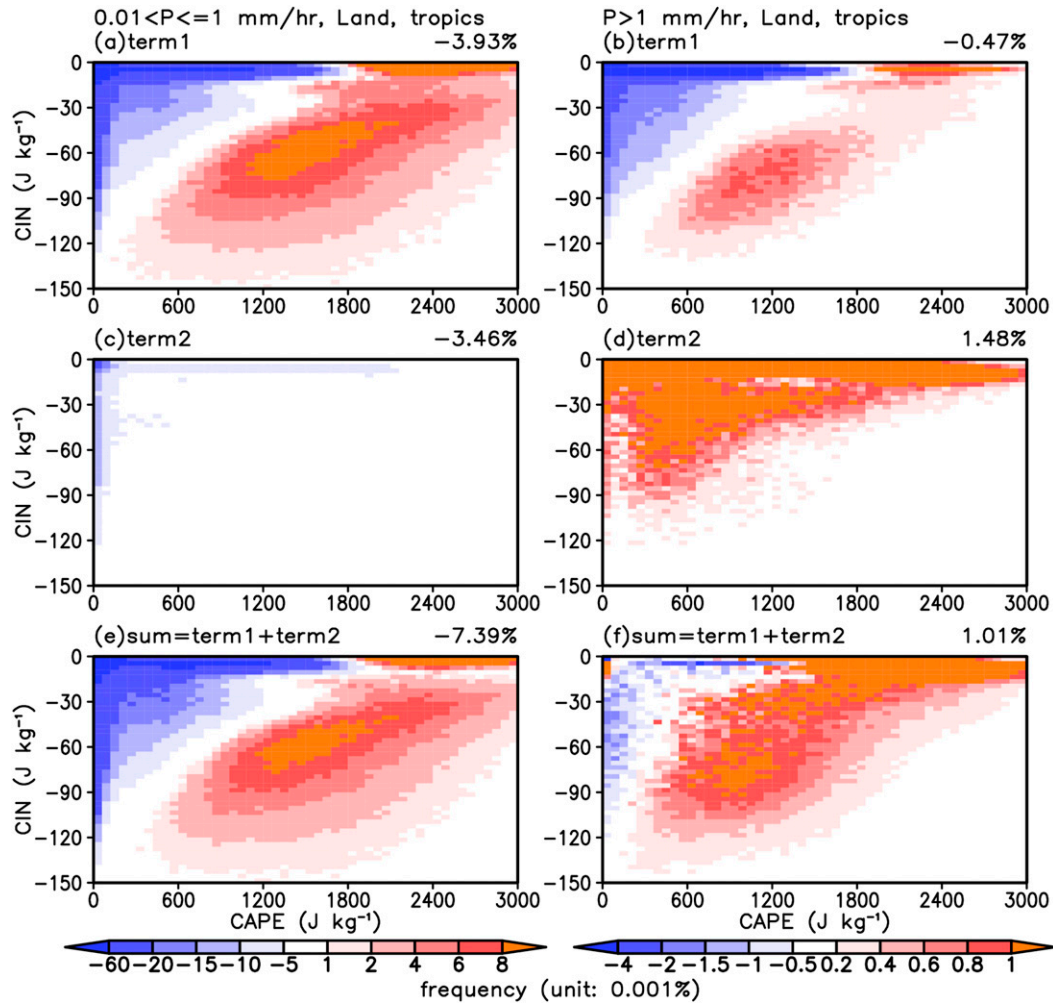


FIG. 12. (left) The two components of the light–moderate precipitation ($0.01 < P \leq 1 \text{ mm h}^{-1}$) frequency change from 1980–99 to 2081–2100 over land in summer (JJA for the Northern Hemisphere and DJF for the Southern Hemisphere) domain in the tropics (20°S – 20°N) due to (a) changes in CAPE and CIN occurrence frequency and (c) changes in the precipitation probability (% of CAPE and CIN occurrences), and (e) their sum from the CCSM4 simulations under the historical and RCP8.5 scenario. (right) As in the left panels, but for precipitation larger than 1 mm h^{-1} . The total frequency averaged over all bins is shown on the top-right corner of each panel.

interval in millimeters per hour to derive the frequency and normalized the frequency to units of percentage probability per 1 mm h^{-1} (instead of units of % frequency per equal $\log_{10}P$ value as in our Fig. 15), which resulted in exponentially decreasing histograms with no peaks. For characterizing light–moderate precipitation, using a constant $\log_{10}P$ bin interval may be more appropriate as it reveals more details at low intensities, although both methods yield increased frequency for heavy precipitation. However, no peaks exist in the histograms over the subtropical ocean (Fig. 15d) and a peak around a very small intensity (~ 0.02 – 0.03 mm h^{-1}) exists over the mid-latitude ocean (Fig. 15f). Thus, a shift toward the right hand of the precipitation histograms induced by a uniform percentage increase in precipitation intensity can generally

lead to fewer light–moderate precipitation events (except for the subtropical ocean) and more heavy precipitation events; this is qualitatively consistent with the decreased (increased) probability for light–moderate (heavy) precipitation as shown in Figs. 10 and 11.

In contrast, Fig. 3 includes the impacts from all possible processes, including the shift induced by the intensity change shown in Fig. 15 and that resulting from the CAPE/CIN frequency changes [term1 in Eq. (4)]. The right-hand shift is much larger in Fig. 15 than in Fig. 3, while the downward (upward) shift for the light–moderate (moderate–heavy) precipitation is smaller (larger) in Fig. 15 than in Fig. 3. As a result, the decrease in the light–moderate precipitation is much larger in Fig. 3 than in Fig. 15, while the increase in the moderate–heavy

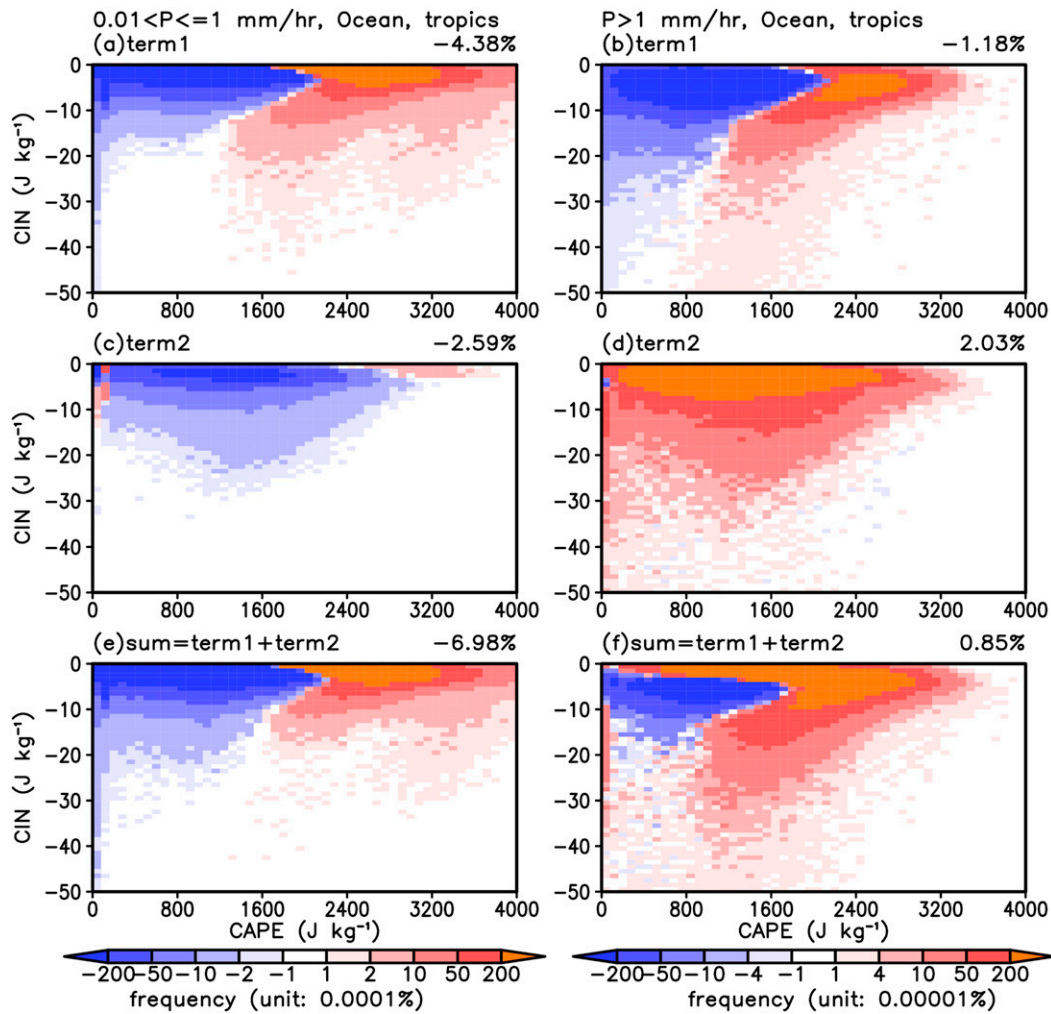


FIG. 13. As in Fig. 12, but for tropical oceans.

precipitation is much smaller in Fig. 3 than in Fig. 15. Thus, although the uniform intensity increase induced by water vapor can help explain some of the model-simulated precipitation frequency changes, other processes may also play an important role, as also suggested by Dai et al. (2017). These may include the impact from CAPE/CIN frequency changes (Chen et al. 2020) on the overall precipitation frequency [term1 in Eq. (4)].

d. Decomposition as a function of precipitation intensity

In section 4b we analyzed the regional precipitation frequency changes and the two decomposed terms as a function of both CAPE and CIN only for two intensity categories: light-moderate precipitation and heavy precipitation. In this section, we will do similar analyses but for more categories of the precipitation intensity (i.e., using the constant $\log_{10}P$ bins) and integrated over all the

plotted CAPE and CIN values. Over the three land areas, the simulated total frequency change for each precipitation intensity bin is estimated by integrating the precipitation frequency change as a function of CAPE and CIN (i.e., $0 < \text{CAPE} \leq 3000 \text{ J kg}^{-1}$ and $-150 \text{ J kg}^{-1} \leq \text{CIN} < 0$, as in Fig. 8). The values of term1 and term2 in Eq. (4) and their sum are also estimated by integrating the precipitation frequency over the same CAPE and CIN range as in Fig. 12. Similar estimates were also made over the three ocean areas but for a different CAPE and CIN range: $0 < \text{CAPE} \leq 4000 \text{ J kg}^{-1}$ and $-50 \text{ J kg}^{-1} \leq \text{CIN} < 0$. These estimates for different precipitation intensity bins allow us to show the distributions (Fig. 16) of the simulated frequency change, the contribution by each of the two decomposed terms, and their sum integrated over all the CAPE/CIN cases (within the stated ranges) in Eq. (4). These distributions reveal the different

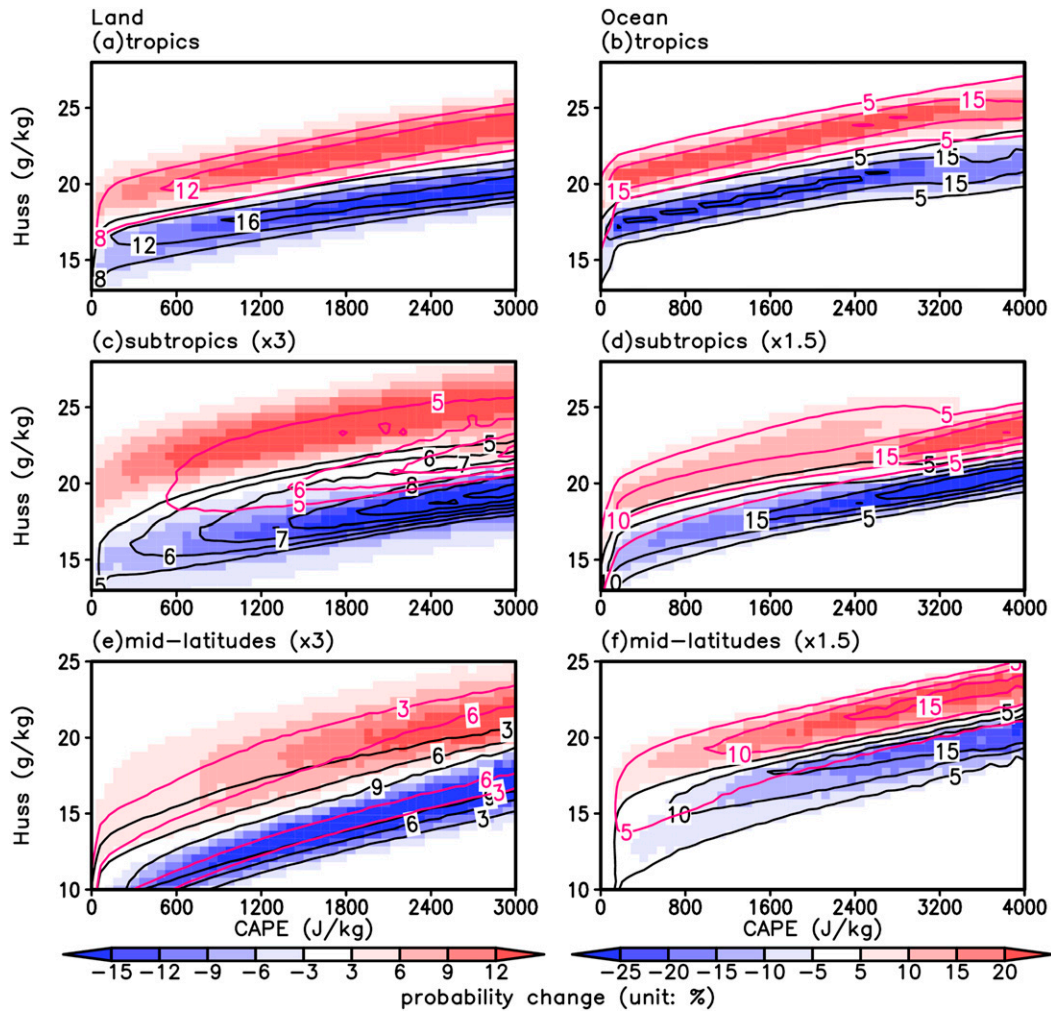


FIG. 14. The occurrence probability (contours; %) of near-surface specific humidity (Huss) during 1980–99 (black) and 2081–2100 (magenta) as a function of CAPE over (a),(c),(e) land and (b),(d),(f) ocean in different regions for summer (JJA for the Northern Hemisphere and DJF for the Southern Hemisphere), and its change [color shading; %; multiplied by a factor of 3 in (c) and (e) or a factor of 1.5 in (d) and (f) in order to use the same scale as that for (a) or (b)] from 1980–99 to 2081–2100, derived using 6-hourly CAPE and Huss data from CCSM4 simulations under the historical and RCP8.5 scenario. A fixed bin number of 50 and 30 was used for CAPE and Huss, respectively.

contributions of term1 and term2 to the precipitation frequency change at every intensity category for all the CAPE/CIN cases.

The distributions of the frequency changes integrated over the examined CAPE and CIN ranges (gray bars in Fig. 16) are qualitatively similar to the frequency changes directly calculated using the 3-hourly precipitation data from the model simulations (gray bars in Fig. 3), although the changes for the very light precipitation events are the opposite over the tropical and subtropical oceans. This indicates that our estimation by integrating frequency changes (estimated as a function of CAPE and CIN) over the limited CAPE and CIN values is reliable and adequate for

analyzing the contributions of the two terms. On the one hand, the sum of the two terms (blue lines in Fig. 16) are comparable to the integrated frequency changes (gray bars in Fig. 16), which confirms the reliability of the decomposition method. On the other hand, our decomposition implies that term1 (due to changes in CAPE and CIN occurrence frequency) generally leads to large decreases in light–moderate precipitation, while term2 (due to changes in precipitation probability under given CAPE and CIN conditions) leads to large decreases in moderate precipitation but increases in heavy and very light precipitation (Fig. 16). Thus, the increased frequency for heavy precipitation

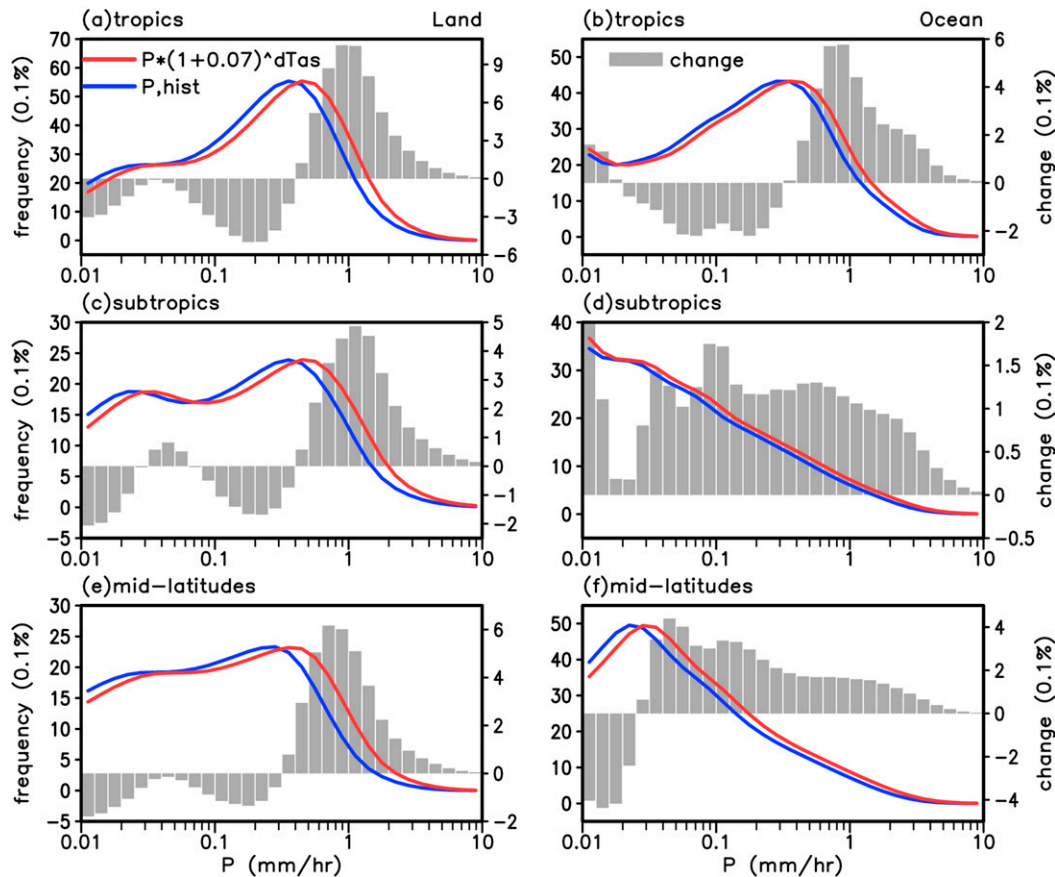


FIG. 15. As in Fig. 3, but with the future histograms (red lines) being estimated using the current P at each grid box multiplied by a factor of $(1 + 0.07)^{dTAs}$, where $dTAs$ is the 2081–2100 minus 1980–99 difference of the summer mean near-surface air temperature at the grid box.

results from the probability change term, confirming the results shown in Figs. 12 and 13.

The broad similarity between the distributions of term2 (Fig. 16) and the frequency changes due to the rightward shift (Fig. 15) over the land areas and tropical ocean suggests that term2 may roughly represent the frequency changes induced by the uniform increase in precipitation intensity, as we already suggested in section 4c. The precipitation probability over different intensity categories would change when the precipitation intensity from all precipitation events is increased by a similar percentage due to increased moisture convergence resulting from increased q . This moisture convergence-induced change in precipitation intensity may be considered as another thermodynamics-induced change to the precipitation histogram, in addition to the changes induced by CAPE/CIN frequency changes. In other words, the impacts of the changes in T and q may be decomposed into 1) the impact through changes in CAPE and CIN occurrence frequency and 2) the impact directly through changes in precipitation intensity.

Both effects would result in the precipitation frequency changes in the future.

5. Summary and discussion

In this study, we first examined the model’s performance in simulating the mean precipitation frequency as compared to TRMM 3B42 and ERA-Interim using 3-hourly data. The CCSM4 model approximately captures the observed spatial patterns in the mean precipitation frequencies for both light–moderate ($0.01 < P \leq 1 \text{ mm h}^{-1}$) and heavy ($P > 1 \text{ mm h}^{-1}$) precipitation. Then we analyzed the model-projected future precipitation changes by comparing the frequencies for two periods: 1980–99 in the all-forcing historical simulation and 2081–2100 under the RCP8.5 high emissions scenario. Light–moderate precipitation is projected to decrease over most of the low to midlatitudes while heavy precipitation would increase over many areas of the globe. The decreased light–moderate precipitation (except for the increased very light precipitation over

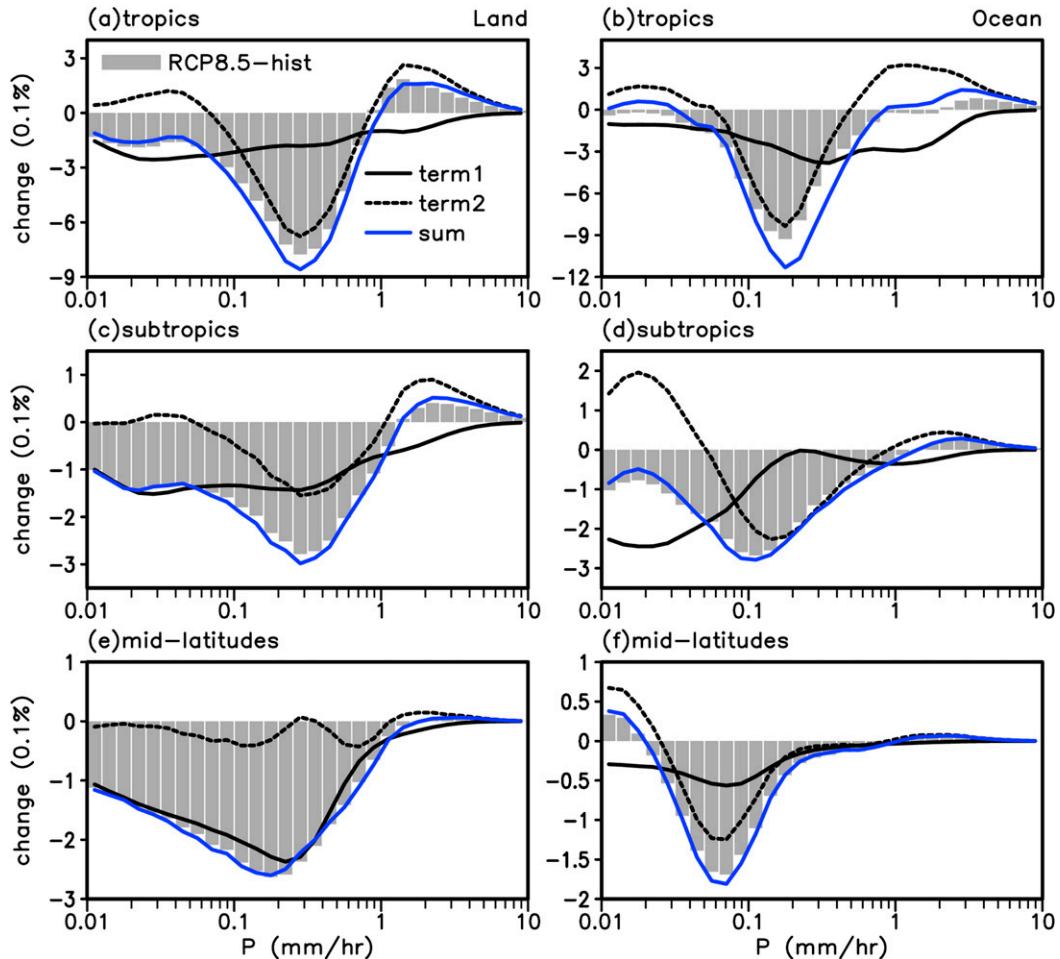


FIG. 16. (left) The logarithmic precipitation frequency change (with a bin size of 0.1 for $\log_{10}P$; gray bars; 0.1% of time) from 1980–99 to 2081–2100 over land in summer (JJA for the Northern Hemisphere and DJF for the Southern Hemisphere) within three latitude zones, and the estimated two components of the precipitation frequency changes (0.1% of time) due to changes in CAPE and CIN occurrence frequency [term1 in Eq. (4); black solid lines] and changes in the precipitation probability (term2; black dotted lines), and their sum (blue solid lines) based on the CCSM4 simulations under the historical and RCP8.5 scenario. All the estimated frequency changes are integrated over limited CAPE and CIN values for $0 < \text{CAPE} \leq 3000 \text{ J kg}^{-1}$ and $-150 \text{ J kg}^{-1} \leq \text{CIN} < 0$. The latitudinal zones include the (a),(b) tropics (20°S – 20°N), (c),(d) subtropics (20° – 40°S/N), and (e),(f) midlatitudes (40° – 60°S/N). (right) As in the left panels, but for oceans with all the estimated frequency changes integrated over limited CAPE and CIN values for $0 < \text{CAPE} \leq 4000 \text{ J kg}^{-1}$ and $-50 \text{ J kg}^{-1} \leq \text{CIN} < 0$.

oceans) and increased heavy precipitation are consistent features over different land and ocean areas and among other climate models (Sun et al. 2007; Pendergrass and Hartmann 2014b; Dai et al. 2018). CAPE and CIN values during the same periods were calculated using 6-hourly temperature T and specific humidity q profiles, and the linkages between the projected changes in precipitation frequency and CAPE or CIN are examined. Significant correlations between the precipitation frequency or intensity and the CAPE or CIN are seen in both the model and ERA-Interim, which implies a link between precipitation and CAPE or CIN.

As shown by Chen et al. (2020), cases with small CAPE and/or CIN are projected to decrease while cases with moderate–strong CAPE and/or CIN would increase in the future over all land areas as CAPE and CIN shift toward higher values under increasing T and q and small changes in RH. Over land areas (and similarly over oceans), light–moderate precipitation events occur most frequently under weak CAPE and/or weak CIN conditions, which are projected to decrease greatly. This results in large decreases (small increases) in light–moderate precipitation frequency under weak (moderate–strong) CAPE and CIN conditions, leading

to overall decreased frequency. For heavy precipitation, the increased frequency under moderate–strong CAPE and CIN overwhelms the decreased frequency under small CAPE and CIN, leading to overall increased frequency in the future.

We further decomposed the precipitation frequency change as a function of CAPE and CIN into two terms [Eq. (4)]: term1 due to changes in the occurrence frequency of CAPE and CIN and term2 due to changes in precipitation probability under given CAPE and CIN. Results show that the decreases in light–moderate precipitation over land result primarily from fewer events with low CAPE and/or low CIN (due to a shift toward higher CAPE and CIN as T and q increase and RH changes little) and second from the decreased precipitation probability. The increases in heavy precipitation over land result mainly from the increased precipitation probability, while the changes in CAPE and CIN frequency offsets the probability-induced increases under low-CAPE and/or low-CIN conditions but slightly enhances the increases under moderate–strong CAPE and/or CIN conditions. The results over oceans are qualitatively similar to those over land.

Increases in water vapor would lead to increased moisture convergence for all precipitation events, which in turn could lead to a uniform percentage increase in precipitation intensity for all events. Such a water vapor–induced intensity change would shift the precipitation histogram toward higher intensity with little change in the shape, leading to decreases (increases) in light–moderate (moderate–heavy) precipitation frequency as the historical histogram peaks around an intensity of 0.3 mm h^{-1} . Such a change mainly represents the precipitation probability-induced change (term2) and it helps explain the decreased (increased) probability of light–moderate (heavy) precipitation in the future climate (Figs. 10 and 11).

In summary, our CCSM4 results show that changes in light–moderate precipitation are dominated by the changes in the occurrence frequency of CAPE and CIN [i.e., term1 in Eq. (4)], while changes in heavy precipitation are determined by both the probability increases (under given CAPE/CIN) and the CAPE/CIN frequency change (i.e., both term2 and term1). More specifically, large decreases in the weak-CAPE and/or weak-CIN cases lead to decreased light–moderate precipitation frequency, while the increased probability for heavy precipitation under given CAPE/CIN offsets most of the decreased heavy precipitation frequency under low-CAPE and/or low-CIN (induced by term1) and results in an overall increase in heavy precipitation. Furthermore, the increased (decreased)

probability for heavy (light–moderate) precipitation under given CAPE and CIN likely results from a shift of the precipitation histogram toward higher intensity due to a uniform percentage increase in precipitation intensity that could result from increased low-level moisture convergence.

Although the CCSM4-simulated mean precipitation frequency distributions are broadly comparable to TRMM 3B42 and ERA-Interim, and the precipitation versus CAPE/CIN relationship is similar to that seen in ERA-Interim, the linkage between the projected changes in precipitation and CAPE/CIN may be model dependent. In particular, how a model links its precipitation to CAPE/CIN (e.g., through its cumulus scheme) may have a major impact on the linkage between the two. As mentioned in section 2, in the ZM95 scheme used in the CCSM4, convective precipitation is linked to $(\text{CAPE} + \text{CIN})$ through the cloud-base mass flux $M_b = (\text{CAPE} + \text{CIN})/(\tau \times F)$. Clearly, such a relationship may not exist in other climate models. It would be interesting to see whether our CCSM4-based results would still hold in other global climate models or regional convection-permitting models (Liu et al. 2017) with different links to CAPE/CIN. Nevertheless, given the overall similarity in the correlations of precipitation with CAPE or CIN between the CCSM4 and ERA-Interim (which does not use the ZM95 scheme), and the similar decreases in light–moderate precipitation and increases in heavy precipitation in other climate models (Sun et al. 2007; Pendergrass and Hartmann 2014b; Dai et al. 2018), and the broad similarity of the CAPE and CIN changes between the CCSM4 and high-resolution convection-permitting simulations over the United States (Rasmussen et al. 2017; Chen et al. 2020), we tend to think that many of the linkages between the precipitation and CAPE/CIN changes discussed above may be qualitatively similar in other climate models. This may be true especially for those aspects related to the impacts from increased water vapor (such as Fig. 15), which is a robust response among climate models (Held and Soden 2000; Collins et al. 2013).

Acknowledgments. We thank the NCAR modeling groups who made the CCSM4 simulations available to us. Zhang and Chen were supported by the National Natural Science Foundation of China (41621005). Chen also acknowledges the support from the China Scholarship Council to sponsor her visit to University at Albany. Dai acknowledges the funding support from the U.S. National Science Foundation (Grant OISE-1743738) and the U.S. National Oceanic and Atmospheric Administration (Awards NA15OAR4310086 and NA18OAR4310425).

REFERENCES

- Adams, D. K., and E. P. Souza, 2009: CAPE and convective events in the Southwest during the North American monsoon. *Mon. Wea. Rev.*, **137**, 83–98, <https://doi.org/10.1175/2008MWR2502.1>.
- Allen, J. T., D. J. Karoly, and K. J. Walsh, 2014: Future Australian severe thunderstorm environments. Part II: The influence of a strongly warming climate on convective environments. *J. Climate*, **27**, 3848–3868, <https://doi.org/10.1175/JCLI-D-13-00426.1>.
- Barkidija, S., and Ž. Fuchs, 2013: Precipitation correlation between convective available potential energy, convective inhibition and saturation fraction in middle latitudes. *Atmos. Res.*, **124**, 170–180, <https://doi.org/10.1016/j.atmosres.2012.12.010>.
- Barthlott, C., C. Hauck, N. Kalthoff, and C. Kottmeier, 2011: Soil moisture impacts on convective indices and precipitation over complex terrain. *Meteor. Z.*, **20**, 185–197, <https://doi.org/10.1127/0941-2948/2011/0216>.
- Chen, D., and A. Dai, 2018: Dependence of estimated precipitation frequency and intensity on data resolution. *Climate Dyn.*, **50**, 3625–3647, <https://doi.org/10.1007/s00382-017-3830-7>.
- , and —, 2019: Precipitation characteristics in the Community Atmosphere Model and their dependence on model physics and resolution. *J. Adv. Model. Earth Syst.*, **11**, 2352–2374, <https://doi.org/10.1029/2018MS001536>.
- Chen, J., A. Dai, and Y. Zhang, 2019: Projected changes in daily variability and seasonal cycle of near-surface air temperature over the globe during the 21st century. *J. Climate*, **32**, 8537–8561, <https://doi.org/10.1175/JCLI-D-19-0438.1>.
- , —, —, and K. L. Rasmussen, 2020: Changes in convective available potential energy and convective inhibition under global warming. *J. Climate*, **33**, 2025–2050, <https://doi.org/10.1175/JCLI-D-19-0461.1>.
- Collins, M., and Coauthors, 2013: Long-term climate change: Projections, commitments and irreversibility. *Climate Change 2013: The Physical Science Basis*, T. F. Stocker et al., Eds., Cambridge University Press, 1029–1136.
- Dai, A., 2001: Global precipitation and thunderstorm frequencies. Part I: Seasonal and interannual variations. *J. Climate*, **14**, 1092–1111, [https://doi.org/10.1175/1520-0442\(2001\)014<1092:GPATFP>2.0.CO;2](https://doi.org/10.1175/1520-0442(2001)014<1092:GPATFP>2.0.CO;2).
- , 2006: Precipitation characteristics in eighteen coupled climate models. *J. Climate*, **19**, 4605–4630, <https://doi.org/10.1175/JCLI3884.1>.
- , X. Lin, and K. L. Hsu, 2007: The frequency, intensity, and diurnal cycle of precipitation in surface and satellite observations over low- and mid-latitudes. *Climate Dyn.*, **29**, 727–744, <https://doi.org/10.1007/s00382-007-0260-y>.
- , R. M. Rasmussen, C. Liu, K. Ikeda, and A. F. Prein, 2017: A new mechanism for warm-season precipitation response to global warming based on convection-permitting simulations. *Climate Dyn.*, <https://doi.org/10.1007/s00382-017-3787-6>.
- , T. Zhao, and J. Chen, 2018: Climate change and drought: A precipitation and evaporation perspective. *Curr. Climate Change Rep.*, **4**, 301–312, <https://doi.org/10.1007/s40641-018-0101-6>.
- Davies, J. M., 2004: Estimations of CIN and LFC associated with tornadic and nontornadic supercells. *Wea. Forecasting*, **19**, 714–726, [https://doi.org/10.1175/1520-0434\(2004\)019<0714:EOCALA>2.0.CO;2](https://doi.org/10.1175/1520-0434(2004)019<0714:EOCALA>2.0.CO;2).
- Dee, D. P., and Coauthors, 2011: The ERA-Interim reanalysis: Configuration and performance of the data assimilation system. *Quart. J. Roy. Meteor. Soc.*, **137**, 553–597, <https://doi.org/10.1002/qj.828>.
- DeMott, C. A., and D. A. Randall, 2004: Observed variations of tropical convective available potential energy. *J. Geophys. Res.*, **109**, D02102, <https://doi.org/10.1029/2003JD003784>.
- Diffenbaugh, N. S., M. Scherer, and R. J. Trapp, 2013: Robust increases in severe thunderstorm environments in response to greenhouse forcing. *Proc. Natl. Acad. Sci. USA*, **110**, 16 361–16 366, <https://doi.org/10.1073/pnas.1307758110>.
- Donat, M. G., A. L. Lowry, L. V. Alexander, P. A. O’Gorman, and N. Maher, 2016: More extreme precipitation in the world’s dry and wet regions. *Nat. Climate Change*, **6**, 508–513, <https://doi.org/10.1038/nclimate2941>.
- Doswell, C. A., III, 1987: The distinction between large-scale and mesoscale contribution to severe convection: A case study example. *Wea. Forecasting*, **2**, 3–16, [https://doi.org/10.1175/1520-0434\(1987\)002<0003:TDBLSA>2.0.CO;2](https://doi.org/10.1175/1520-0434(1987)002<0003:TDBLSA>2.0.CO;2).
- , and E. N. Rasmussen, 1994: The effect of neglecting the virtual temperature correction on CAPE calculations. *Wea. Forecasting*, **9**, 625–629, [https://doi.org/10.1175/1520-0434\(1994\)009<0625:TEONTV>2.0.CO;2](https://doi.org/10.1175/1520-0434(1994)009<0625:TEONTV>2.0.CO;2).
- ECMWF, 2011: ERA-Interim. Accessed 1 December 2018, <https://www.ecmwf.int/en/forecasts/datasets/reanalysis-datasets/era-interim>.
- Ellis, T. D., T. L’Ecuyer, J. M. Haynes, and G. L. Stephens, 2009: How often does it rain over the global oceans? The perspective from CloudSat. *Geophys. Res. Lett.*, **36**, L03815, <https://doi.org/10.1029/2008GL036728>.
- Gent, P. R., and Coauthors, 2011: The Community Climate System Model version 4. *J. Climate*, **24**, 4973–4991, <https://doi.org/10.1175/2011JCLI4083.1>.
- Held, I. M., and B. J. Soden, 2000: Water vapor feedback and global warming. *Annu. Rev. Energy Environ.*, **25**, 441–475, <https://doi.org/10.1146/annurev.energy.25.1.441>.
- Holley, D. M., S. R. Dorling, C. J. Steele, and N. Earl, 2014: A climatology of convective available potential energy in Great Britain. *Int. J. Climatol.*, **34**, 3811–3824, <https://doi.org/10.1002/joc.3976>.
- Huang, D., P. Yan, X. Xiao, J. Zhu, X. Tang, A. Huang, and J. Cheng, 2019: The tri-pole relation among daily mean temperature, atmospheric moisture and precipitation intensity over China. *Global Planet. Change*, **179**, 1–9, <https://doi.org/10.1016/j.gloplacha.2019.04.016>.
- Huffman, G. J., and Coauthors, 2007: The TRMM Multisatellite Precipitation Analysis (TMPA): Quasi-global, multiyear, combined-sensor precipitation estimates at fine scales. *J. Hydrometeorol.*, **8**, 38–55, <https://doi.org/10.1175/JHM560.1>.
- Johns, R. H., and C. A. Doswell III, 1992: Severe local storms forecasting. *Wea. Forecasting*, **7**, 588–612, [https://doi.org/10.1175/1520-0434\(1992\)007<0588:SLSF>2.0.CO;2](https://doi.org/10.1175/1520-0434(1992)007<0588:SLSF>2.0.CO;2).
- Lau, W. K.-M., and H.-T. Wu, 2007: Detecting trends in tropical rainfall characteristics, 1979–2003. *Int. J. Climatol.*, **27**, 979–988, <https://doi.org/10.1002/joc.1454>.
- , —, and K.-M. Kim, 2013: A canonical response of precipitation characteristics to global warming from CMIP5 models. *Geophys. Res. Lett.*, **40**, 3163–3169, <https://doi.org/10.1002/grl.50420>.
- Lee, S.-M., and H.-R. Byun, 2011: Distribution of convective energy at upper level in South Korea and the possibility of artificial showery rain caused by activated CAPE. *Theor. Appl. Climatol.*, **105**, 537–551, <https://doi.org/10.1007/s00704-011-0408-x>.
- Liu, C., and Coauthors, 2017: Continental-scale convection-permitting modeling of the current and future climate of North America. *Climate Dyn.*, **49**, 71–95, <https://doi.org/10.1007/s00382-016-3327-9>.

- Liu, S.-C., C. Fu, C.-J. Shiu, J.-P. Chen, and F. Wu, 2009: Temperature dependence of global precipitation extremes. *Geophys. Res. Lett.*, **36**, L17702, <https://doi.org/10.1029/2009GL040218>.
- Ma, S., T. Zhou, A. Dai, and Z. Han, 2015: Observed changes in the distributions of daily precipitation frequency and amount over China from 1960 to 2013. *J. Climate*, **28**, 6960–6978, <https://doi.org/10.1175/JCLI-D-15-0011.1>.
- , and Coauthors, 2017: Detectable anthropogenic shift toward heavy precipitation over eastern China. *J. Climate*, **30**, 1381–1396, <https://doi.org/10.1175/JCLI-D-16-0311.1>.
- McBride, J., and W. Frank, 1999: Relationships between stability and monsoon convection. *J. Atmos. Sci.*, **56**, 24–36, [https://doi.org/10.1175/1520-0469\(1999\)056<0024:RBSAMC>2.0.CO;2](https://doi.org/10.1175/1520-0469(1999)056<0024:RBSAMC>2.0.CO;2).
- Monkam, D., 2002: Convective available potential energy (CAPE) in Northern Africa and tropical Atlantic and study of its connections with rainfall in Central and West Africa during summer 1985. *Atmos. Res.*, **62**, 125–147, [https://doi.org/10.1016/S0169-8095\(02\)00006-6](https://doi.org/10.1016/S0169-8095(02)00006-6).
- Myoung, B., and J. W. Nielsen-Gammon, 2010a: Sensitivity of monthly convective precipitation to environmental conditions. *J. Climate*, **23**, 166–188, <https://doi.org/10.1175/2009JCLI2792.1>.
- , and —, 2010b: The convective instability pathway to warm season drought in Texas. Part I: The role of convective inhibition and its modulation by soil moisture. *J. Climate*, **23**, 4461–4473, <https://doi.org/10.1175/2010JCLI2946.1>.
- Neale, R. B., and Coauthors, 2010: Description of the NCAR Community Atmosphere Model (CAM 4.0). NCAR Tech. Note NCAR/TN-485+STR, 212 pp., www.cesm.ucar.edu/models/ccsm4.0/cam/docs/description/cam4_desc.pdf.
- Pendergrass, A. G., and D. L. Hartmann, 2014a: Two modes of change of the distribution of rain. *J. Climate*, **27**, 8357–8371, <https://doi.org/10.1175/JCLI-D-14-00182.1>.
- , and —, 2014b: Changes in the distribution of rain frequency and intensity in response to global warming. *J. Climate*, **27**, 8372–8383, <https://doi.org/10.1175/JCLI-D-14-00183.1>.
- Prein, A. F., R. M. Rasmussen, K. Ikeda, C. Liu, M. P. Clark, and G. J. Holland, 2017: The future intensification of hourly precipitation extremes. *Nat. Climate Change*, **7**, 48–52, <https://doi.org/10.1038/nclimate3168>.
- Rasmussen, K. L., A. F. Prein, R. M. Rasmussen, K. Ikeda, and C. Liu, 2017: Changes in the convective population and thermodynamic environments in convection-permitting regional climate simulations over the United States. *Climate Dyn.*, <https://doi.org/10.1007/s00382-017-4000-7>.
- Seeley, J. T., and D. M. Romps, 2015a: The effect of global warming on severe thunderstorms in the United States. *J. Climate*, **28**, 2443–2458, <https://doi.org/10.1175/JCLI-D-14-00382.1>.
- , and —, 2015b: Why does tropical convective available potential energy (CAPE) increase with warming? *Geophys. Res. Lett.*, **42**, 10 429–10 437, <https://doi.org/10.1002/2015GL066199>.
- Shiu, C. J., S. C. Liu, C. Fu, A. Dai, and Y. Sun, 2012: How much do precipitation extremes change in a warming climate? *Geophys. Res. Lett.*, **39**, L17707, <https://doi.org/10.1029/2012GL052762>.
- Singh, M. S., and P. A. O’Gorman, 2013: Influence of entrainment on the thermal stratification in simulations of radiative convective equilibrium. *Geophys. Res. Lett.*, **40**, 4398–4403, <https://doi.org/10.1002/grl.50796>.
- Sobel, A. H., S. E. Yuter, C. S. Bretherton, and G. N. Kiladis, 2004: Large-scale meteorology and deep convection during TRMM KWAJEX. *Mon. Wea. Rev.*, **132**, 422–444, [https://doi.org/10.1175/1520-0493\(2004\)132<0422:LMADCD>2.0.CO;2](https://doi.org/10.1175/1520-0493(2004)132<0422:LMADCD>2.0.CO;2).
- Sun, Y., S. Solomon, A. Dai, and R. Portmann, 2006: How often does it rain? *J. Climate*, **19**, 916–934, <https://doi.org/10.1175/JCLI3672.1>.
- , —, —, and R. W. Portmann, 2007: How often will it rain? *J. Climate*, **20**, 4801–4818, <https://doi.org/10.1175/JCLI4263.1>.
- Taylor, K. E., R. J. Stouffer, and G. A. Meehl, 2012: An overview of CMIP5 and the experiment design. *Bull. Amer. Meteor. Soc.*, **93**, 485–498, <https://doi.org/10.1175/BAMS-D-11-00094.1>.
- Tompkins, A. M., 2001: Organization of tropical convection in low vertical wind shears: The role of water vapor. *J. Atmos. Sci.*, **58**, 529–545, [https://doi.org/10.1175/1520-0469\(2001\)058<0529:OOTCIL>2.0.CO;2](https://doi.org/10.1175/1520-0469(2001)058<0529:OOTCIL>2.0.CO;2).
- Trenberth, K. E., A. Dai, R. M. Rasmussen, and D. B. Parsons, 2003: The changing character of precipitation. *Bull. Amer. Meteor. Soc.*, **84**, 1205–1218, <https://doi.org/10.1175/BAMS-84-9-1205>.
- Wang, J., A. Dai, C. Mears, and L. Zhang, 2016: Global water vapor trend from 1988–2011 and its diurnal asymmetry based on GPS, radiosonde, and microwave satellite measurements. *J. Climate*, **29**, 5205–5222, <https://doi.org/10.1175/JCLI-D-15-0485.1>.
- Zhang, G. J., 2002: Convective quasi-equilibrium in midlatitude continental environment and its effect on convective parameterization. *J. Geophys. Res.*, **107**, 4220, <https://doi.org/10.1029/2001JD001005>.
- , and N. A. McFarlane, 1995: Sensitivity of climate simulations to the parameterization of cumulus convection in the Canadian Climate Centre general circulation model. *Atmos.–Ocean*, **33**, 407–446, <https://doi.org/10.1080/07055900.1995.9649539>.